Investigating the effect of aortic valve inflow profile in ascending thoracic aortic aneurysm

Jan Veer 4652754

Supervisors:
Mathieu Pourquie
Selene Pirola

Delft University of Technology

June 28, 2023

Abstract

Ascending thoracic aortic aneurysm is a dangerous condition which is hard to locate in patients. CFD can be used to assess someone's risk of suffering from such an aneurysm and also to assess any possible relation of an aneurysm with relevant parameters, like the shape of the aorta or how blood flows into the aorta.

Existing research on ascending aortic CFD flow generally focuses on assessing relatively high wall shear stress, seen as the cause for aortic wall damage and aneurysms, in patients and not much on any possible relationships between aortic shape and inflow with ascending aortic aneurysm. Work that does exist often uses 4D flow MRI, shown to produce results regarding peak wall shear stresses with less accuracy compared to CFD.

This thesis aims to supply that information using an aortic geometry from a large dataset of synthetically generated aortas together with synthetically generated inlet velocity profiles, showing a possibility to work without the need for patient measurements. The main work in this thesis focuses on finding any possible relationship between aortic inflow angle and relatively high wall shear stress, such that the results may better explain how aortic inflow can influence the appearance of aneurysms.

For this, a workflow has been established that allows working with large aortic geometry and inflow profile datasets with relative ease. This workflow process uses a mix of OpenFoam and Ansys Fluent usage.

Results have shown that the flow jet angle in the core of the flow has a significant negative correlation with peak WSS within the ascending aorta for the chosen aortic geometry. This is in contrast with other work showing positive correlations with WSS. This may suggest aortic geometry dependence together with the need to look at other flow variables, like jet impingement angle, to explain how aortic inflow can influence high WSS within the ascending aorta.

Recommendations for future work include: The same study but with a focus on aortas of healthy young people to see if aortas at risk can be found, as existing work mainly focuses on old people with ascending thoracic aortic aneurysm, a similar study with a focus on the inclusion of various aortic geometries to find how aortic geometry may influence the effect inflow variables can have on high WSS, the creation of a tool to easily calculate the impingement angle from aortic flow data and research into if aortic jet flow disruption could reduce peak WSS in the ascending aorta for use in aortic reconstruction.

Acknowledgements

I would like to thank my supervisors, Mathieu Pourquie and Selene Pirola, for their help and knowledge throughout the entire thesis.

I would also like to thank Frank Gijsen for his assistance at the start of the thesis, and my family for their support.

Contents

1 Introduction

Ascending thoracic aortic aneurysm (aTAA) is a disease where there is a weak spot in the aorta, such that the aortic walls bulge out and may eventually rupture. This aneurysm affects about 0.01% of the population each year [1] and for many this condition remains hidden leading to 50% of people suffering from aTAA dying early [2]. The exact causes of aTAA development are not clearly understood and gaining a better understanding of it is crucial to prevent death, especially in an aging society with an increasing amount of obesity cases.

Diagnosing aTAA is difficult, as most aTAA cases do not show any symptoms, and is often detected during other health exams [1]. Prediction of someone having or developing aTAA is challenging, as extensive work and resources need to be put in for a single patient to find out if they have aTAA. This includes the use of chest X-rays or MR angiography (MRA) [1]. These techniques also do not work in up to 60% of aTAA cases for the purpose of finding aTAA. High wall shear stress (WSS) has been shown to predict degeneration of thoracic aortic walls [3]. WSS can be measured indirectly with CFD (Computational Fluid Dynamics) and 4D flow MRI to find if someone could be at risk of gaining aTAA, as has been shown with patients with bicuspid aortic valve (BAV) who have elevated WSS compared to people without BAV [4, 5].

Limited research has been conducted on the possible relationship between aortic shape and inflow with high WSS. Research done on the possible shape relationship has shown that aortic arch curvature does influence wall shear stress [6, 7], but there are more shape and inflow parameters that could be tested, which could lead to improved understanding and diagnosis of aTAA development. With the work done in this thesis, a single parameter can be controlled and researched while using realistic inflow profiles and geometries.

The aim of this project is to study the relation between the inflow angle generated by the aortic valve and WSS in aTAA. To achieve this, a selected realistic aortic shape was simulated, using CFD, in combination with 20 different inlet velocity profiles, characterized by different inflow angles. To perform this, a workflow was designed to automate the setup needed to run simulations of any required combination of aortic shape and velocity profiles.

The results show that a higher blood inflow angle is related to lower peak WSS in the ascending aorta. Other work [8] showed the reverse with higher peak WSS. This difference might be related to a difference in aortic shape used which can influence the impingement angle at which blood flows unto a wall, as that has been shown to be related to peak WSS [9]. This impingement angle is generally not reported in similar work, despite its relevance to peak WSS.

2 Literature review

2.1 General knowledge of aorta

2.1.1 Anatomy

The aorta is the largest artery in the human body. It is divided into the thoracic (near the heart) and abdominal areas, see figure 1, starting at the heart and ending into multiple branches. The thoracic aorta is divided into the ascending aorta, aortic arch and the descending aorta. All of the blood needed for the human body is distributed through the aorta by the heart at an approximate rate of 5 liter per minute [10]. Near the opening of the aorta is the aortic valve, which generally consist of three leaflets which function as a one-way valve for blood flowing from the heart to the aorta. The shape of this valve can influence how blood flows into the aorta and partially determine the shape of velocity inflow profiles used in aorta flow as shown (CFD) studies [11, 12].

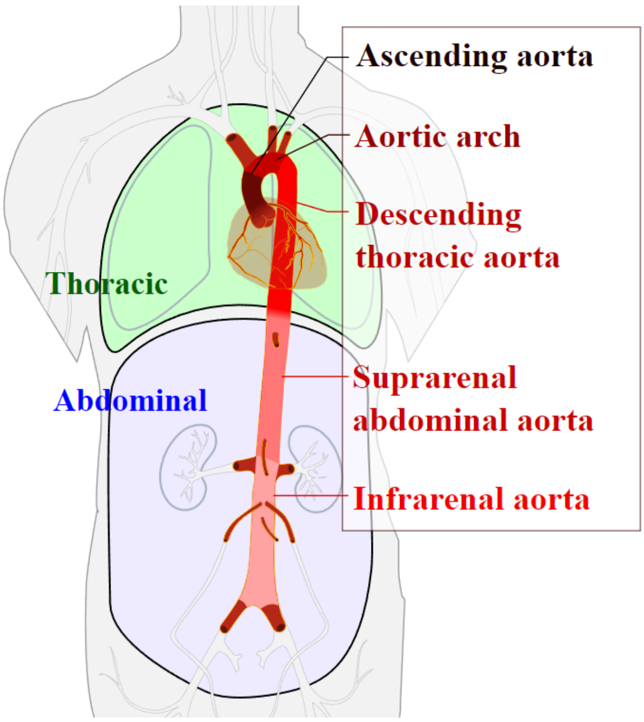

Figure 1: Overall aorta anatomy [13]

This blood flow follows a wave pattern, which can be seen in figure 2. It starts with the opening of the aortic valve, leading to blood flowing into the aorta and an increase in aortic pressure. Then the valve closes and aortic pressure drops until the cycle repeats. The approximate time period when the valve is open and aortic pressure is increasing is called systole, and the other period of lowering aortic pressure is called diastole.

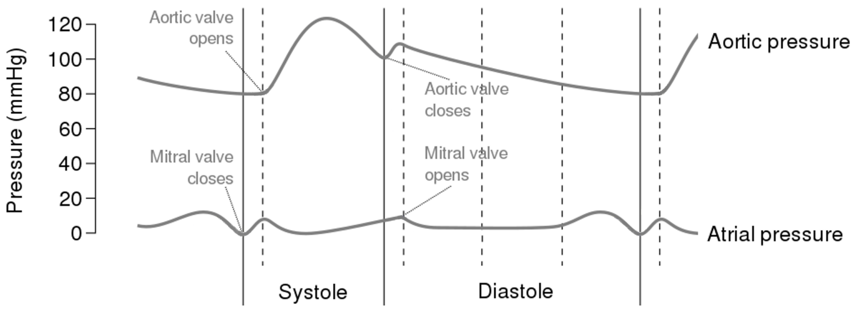

Figure 2: Graph of cardiac cycle's effect on aortic pressure [14]

2.1.2 Geometry

The exact shape of the aorta is subject-specific and the differences in shape affect the flow, which in turn affects WSS and aTAA. A list of geometrical biomarkers from the literature [15] that partially define the shape of the aorta are shown in table 1 and figure 3.

Label	Biomarker description
SoV	Radius of the aorta in the middle of the sinuses of Valsalva (mm)
PA	Radius at a point in the ascending aorta, close to the sinotubular junction (mm)
MA	Radius at a point in mid-ascending aorta (mm)
PT	Radius at a point in the top of the aortic arch (mm)
PD	Radius at a point in the descending aorta, opposite to PA (mm)
LPD	Length of centerline from valve to PD (mm)
k	Mean analytic curvature of the centerline from PA to PD according to the following equation $k_{point} = \sqrt{\left(\frac{d^2x}{ds^2}\right)^2 + \left(\frac{d^2y}{ds^2}\right)^2 + \left(\frac{d^2z}{ds^2}\right)^2}$ where x, y, z are the coordinates of a certain point on the centerline and s being the arc length of the tangent direction [16]
h	Height from PT to the level of PA/PD (mm)
w	Width of the arch, measured as the distance from PA to PD (mm)
h/w	Height-to-width ratio
tor	Tortuosity, defined as $1 - \frac{\mathrm{W}}{\mathrm{LPD}}$

Table 1: Table showing aorta shape biomarkers and their descriptions [15]

The aortic root, the area before the ascending aorta near the inlet and aortic valve, can also be classified into three phenotypes: N, A and E [15], visually described in figure 4. These phenotypes are bases on SoV, PA and MA biomarkers from table 1, and the relation between them is as follows: Phenotype N has SoV $>$ PA and SoV $\geq$ MA, phenotype A has SoV $>$ PA and SoV $<$ MA, and Phenotype E has SoV $\leq$ PA [17]. These phenotype dimensions occur naturally and could have a relationship with WSS and aTAA. There are also additional classifications that include various types of aortic dilation [18], which are not treated here.

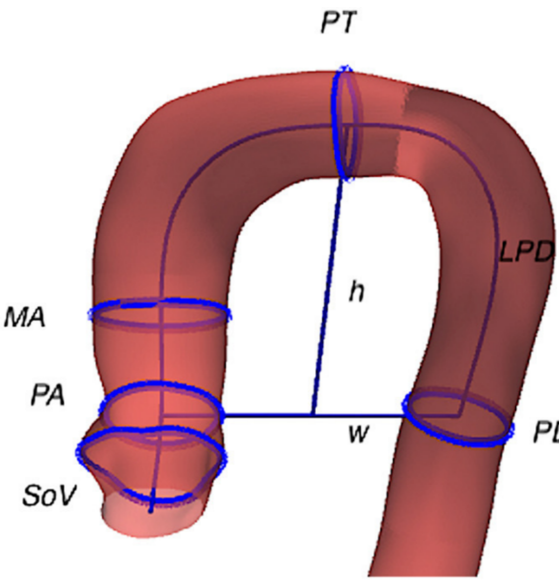

Figure 3: Picture showing aorta shape biomarkers [15]

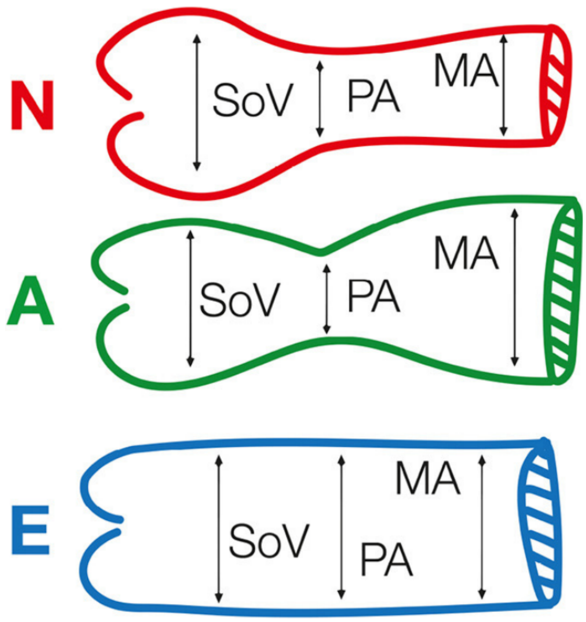

Figure 4: Picture showing ascending aorta phenotypes [15]

Similar studies [7, 19, 6] that research aortic flow and WSS, look at diameters at various locations, aorta shape phenotype (N, A, E), curvature, tortuosity, and orifice area of the aortic valve, but they do not usually correlate WSS results directly with these parameters. They [7, 19] generally use PCA (principal component analysis) to simplify the shape into 'modes'. Callaghan et al. [6] instead focuses on three parameters: Curvature, diameter and 'the angle between the centerline point at the crest of the transverse aortic arch and centerline points 6 cm proximal and distal to this' [6] of the aortic arch and descending aorta.

Callaghan et al. [6] showed that vessel diameter within the aortic arch and descending aorta, and radius of curvature of the aortic arch correlated with significantly with WSS in those areas.

Cosentino et al. [7] showed a correlation between WSS at the sinotubular junction for BAV aTAA, close to PA in figure 3, with a shape mode associated with bulging dilation on the side of the aTAA wall directed to the front of the body.

Thamsen et al. [19] showed mainly the generation and use of a large amount of synthetic aortic geometry and inflow data.

2.1.3 Flow and WSS

The flow within the aorta changes over time during the cardiac cycle. The parts of this cycle with the highest flow through the aorta are the systole and the decelerating systole. These parts are interesting to look at as the peak velocity leads to the highest overall WSS in the aorta [20], and elevated WSS has been shown to associate with wall degradation in aTAA [3] and other biomechanical properties associated with aortic dissection [21]. This is because WSS is directly related to the velocity gradient near the wall and higher average velocity should lead to higher velocity gradient near the aorta walls, see equation 1

$$\tau_W \equiv \tau(y=0) = \mu \frac{\partial u}{\partial y}\bigg|_{y=0} \tag{1}$$

where τ_W is wall shear stress, y is distance from a wall, u is velocity and μ is dynamic viscosity. This simplified version of WSS is derived from shear stress τ being a function of the rate of strain $\frac{d\gamma}{dt}$. For Newtonian fluids (constant viscosity) this function looks like $\tau = \mu\frac{d\gamma}{dt}$, where μ is how much a fluid resists shear deformation, t being the time and γ being the shear strain. For parallel fluid motion, small time scales and small length scales, the rate of strain can be rewritten as the velocity gradient as $\frac{d\gamma}{dt} = \frac{du}{dy}$ with u being the velocity and y being the distance. This leads to $\tau = \mu\frac{du}{dy}$. When this shear stress is near a wall, it can be written like equation 1 [22, 23].

Studies look at transient conditions and look at time-averaged wall shear stress (TAWSS), WSS averaged across a time period like the cardiac cycle, for more realistic results compared to steady state simulations [24, 25, 26, 27], some studies also look at steady state simulations at the peak velocity [7, 28]. Lee et al. [29] has shown that using steady simulation could be good enough as a description of the 'mean' behaviour of the transient pulse flow, including the flow patterns and WSS distribution. A range of observed peak WSS values from these studies can be seen in table 2.

	Max observed WSS	Max observed TAWSS	Notes
Lantz et al.[24]	7 Pa	1 Pa	FSI
Cosentino et al. [7]	21 Pa	-	-
Vinoth et al.[26]	30-45 Pa (Normal vs Diseased)	-	Steady state results. Abdominal aneurysm focus
Pasta et al. [28]	55 Pa	-	FSI. Ascending aorta focus
Lee et al. [29]	20 Pa	-	-
Pasta et al. [27]	22 Pa	8 Pa	aTAA focus

Table 2: Observed peak WSS and TAWSS values from literature

For justifying the use of steady state, the Womersley number, $\alpha = L\left(\frac{\omega\rho}{\mu}\right)^{1/2}$ [30], is often used. Here ω is the angular frequency of oscillations, L is a length scale, ρ is the density of the fluid and μ is the dynamic viscosity of the fluid [30]. For $\alpha < 1$, the flow can be assumed to be quasi-steady [31]. Using the average ascending aortic diameter of 3.2 cm [32] and average resting heart rate of 75 [33] gives a Womersley number of $\alpha = \frac{0.0032}{2}\left(\frac{2\pi\cdot 75\cdot 1000}{0.0035}\right)^{1/2} = 18.6$. Even though the Womersley number is too high to assume quasi-steady flow, other work focusing on shape-WSS relation [7] in the thoracic aorta also use steady state at peak systole flow, presumably to reduce computational cost. An other study by Vincent et al. [31] states that even for a Womersley number of 8, the use of steady state is justified as the sensitivity of WSS to geometry can reasonably be considered independent of how WSS varies in time.

2.1.4 Blood properties

For determining WSS in CFD simulations, the most important blood fluid property to know is its viscosity, see equation 1. Commonly used values for this viscosity in CFD simulations lie between 3.5 and 4.0 mPa·s, however blood shows shear thinning behaviour making its viscosity variable [34]. Blood flow is also multiphase as it is a liquid (plasma) with solid particles, like red and white blood cells. Modelling all the solid particles is generally not possible at blood flow on the scale of the aorta and thus blood is generally treated as single phase liquid [35, 6, 3, 36, 37]. The solid particles have a dimension of approximately 8 micron, making a continuum assumption of blood in the aorta, which has a approximate diameter of 20-30 millimeter, possible [38, 39]. The non-Newtonian behaviour of blood is also caused by the solid particles and usually plays a role at low shear rate and smaller blood vessels [34]. In the aorta this behaviour can generally be neglected because of the high shear rate at systolic peak [39, 40], especially as the areas of interest in this study are high shear regions.

A commonly used non-Newtonian model for blood flow is the Carreau model. This model is a combination of Newtonian and power-law models, capable of describing shear thinning behaviour [41]. The equation for the Carreau model is seen in the following equation 2 [42, 43]

$$\mu = \mu_{\text{inf}} + (\mu_0 - \mu_{\text{inf}}) \left(1 + (\lambda \dot{\gamma}^2)\right)^{\frac{n-1}{2}} \tag{2}$$

with μ being the viscosity dependent on the shear rate $\dot{\gamma}$, μ_0 being the viscosity at zero shear rate, μ_{inf} being the viscosity at infinite shear rate, λ being the characteristic time and n being the power index. The behaviour of this equation is such that at low shear rates the fluid behaves Newtonian with viscosity at μ_0, at high shear rates it also behaves Newtonian with viscosity at μ_{inf} and in between it behaves like a Power-law fluid [42, 43].

Petuchova et al. [44] showed that WSS on an ascending aortic aneurysm surface during systole was 30% higher with a non-Newtonian model as compared to a Newtonian model. This is in contrast with the previous statement that the non-Newtonian behaviour can generally be neglected.

Perktold et al. [45] showed no essential difference between non-Newtonian and Newtonian model for large artery models (with diameter 4 times smaller than the ascending aorta).

Pedley et al. [39] wrote that in unsteady flow non-Newtonian behaviour can become relevant when the shear rate is less than 100 s^{-1}. Within the abdominal aorta (no data for ascending aorta) the shear rate varies between $61s^{-1}$ and $424s^{-1}$ [46], which indicates that a shear rate within the ascending aorta above $100s^{-1}$ is realistic.

There seems to be no consensus on the use of Newtonian or non-Newtonian blood modelling for the aorta and large arteries [47, 45, 48, 26, 44, 39, 36, 37, 40]. Ballyk et al. [47] states that: non-Newtonian (based on generalized power law model) rheology has a significant effect on steady flow WSS while it has minor effect on unsteady flow WSS. Perktold et al. [48] showed that there are no significant differences in flow phenomena and minor differences in WSS for non-Newtonian (Casson) and Newtonian modelling, although only unsteady flow was tested.

Nearly all CFD related work with blood 'assumed' it as an incompressible fluid. A study has shown that blood has a similar compressibility as distilled water [49], which is also considered incompressible under 'normal' circumstances. An example of compressed water is at the bottom of the ocean, where it is compressed by 1.8% at 40 MPa [50], which is very far from the conditions of an aorta.

2.1.5 Aortic walls

In aortic flow, the aorta walls deform in time because of periodic flow within the aorta and the wall not being rigid. For recreating realistic aortic flow, it is preferable to include this wall deformation, as it also has an impact on the flow, which in term has an impact on parameters like WSS. Fluid-structure interaction (FSI) models are however computationally very expensive compared to using rigid walls in CFD simulations, which makes them impractical for simulating multiple different aorta CFD cases [40]. Hence, the majority of aorta CFD studies assume a rigid aortic wall. Another reason why rigid walls are often used is that patient-specific arterial wall properties are difficult to obtain and often are unknown [40].

It has been shown that the influence of using FSI in aorta CFD simulations is low on TAWSS, while for instantaneous WSS it can have a significant impact [24] and that the use of rigid walls in general can cause overestimation of WSS [51]. Lantz et al. [24] showed that instantaneous WSS values could differ by about 2 times (in a range of 1 to 3 Pa) in low and high WSS areas when comparing the use of FSI and rigid walls, although most differences were seen in the descending aorta.

2.2 Good CFD practice

CFD is used to simulate fluid flow. This section will mostly show what is done in the literature to simulate aortic flow with CFD.

2.2.1 Governing equations

The governing equations for fluid dynamics problems are the continuity equations and momentum (Navier-Stokes) equations. Fluent, the main CFD simulation software used, defines the continuity equation as [52]:

$$\frac{\partial \rho}{\partial t} + \nabla \cdot (\rho \vec{v}) = S_m \tag{3}$$

where S_m is a source term for mass added in from a dispersed second phase, which is irrelevant for this thesis. This equation explains that the difference of the mass inflow rate of a system and the mass outflow rate of a system ($\nabla \cdot (\rho \vec{v})$) is equal to the negative accumulation of mass in the system over time ($\frac{\partial \rho}{\partial t}$), excluding the S_m source term [53]. As this thesis uses an incompressible fluid for the simulations, the continuity equation can be simplified to $\nabla \cdot \vec{v} = 0$ because of ρ being constant for these equations.

The momentum conservation equations are defined by Fluent as the following [52]:

$$\frac{\partial}{\partial t}(\rho \vec{v}) + \nabla \cdot (\rho \vec{v}\vec{v}) = -\nabla p + \nabla \cdot (\bar{\bar{\tau}}) + \rho \vec{g} + \vec{F} \tag{4}$$

where p is the static pressure, $\bar{\bar{\tau}}$ is the stress tensor, $\rho \vec{g}$ is the gravitational body force and $\vec{F}$ are external body forces [52]. $\vec{F}$ is unused in this thesis. For an incompressible fluid, this can be further written as [54]:

$$\frac{\partial \vec{v}}{\partial t} + (\vec{v} \cdot \nabla)\vec{v} - \nu \nabla^2 \vec{v} = -\nabla \left(\frac{p}{\rho_0} \right) + \vec{g} \tag{5}$$

with ν being the kinematic viscosity, ρ_0 being the constant density used and excluding $\vec{F}$. In this equation $\frac{\partial \vec{v}}{\partial t}$ is the change in velocity over time, $\nabla \cdot (\rho \vec{v}\vec{v})$ is the transport of momentum (convection term), $\nu \nabla^2 \vec{v}$ is the diffusion of flow caused by internal stress, $-\nabla \left(\frac{p}{\rho_0} \right)$ is the pressure gradient and $\vec{g}$ are external body forces, like gravity.

For the finite volume method, used in CFD, the equations are integrated across mesh cell volumes (see section 2.2.2) and discretized to form a system of equations for every mesh cell used. The software used will solve the system of equations with iterations until it reaches a preset tolerance for the error in the equations.

2.2.2 Mesh

For CFD simulations a mesh is required for the desired working geometry, like the inside of a pipe for pipe flow. The mesh divides the geometry into many small 3D cells (if working with 3D geometry). The governing fluid dynamics equations are solved for each cell in relation to adjacent cells. The quality of a mesh is important, as even a couple of broken mesh cells in a group of millions of cells can break a simulation. The quality is also important for the accuracy of the solution and fast convergence.

For the mesh it is important to use small elements near any locations that could have large change of velocity gradients, especially walls, as accurate WSS results depend on being able to evaluate the velocity gradient values near the wall properly [34], which is not possible if the elements are too large and do not capture the velocity gradient in enough detail. To find a mesh size that is good enough, often multiple inflation layers of mesh elements are used on the aorta walls [19, 55], together with a mesh sensitivity analysis [19, 34, 55]. The inflation layers are also used for capturing the boundary layer and controlling y+, see equation 6. The mesh sensitivity analysis compares results of the same simulations but with a decreasing mesh size until it reaches convergence. The final results have less than 3% difference compared to the results of the previous mesh size tested. This final result would be considered 'mesh independent' [34]. This usually leads to meshes with an amount of cells in the order of millions for the aorta.

When determining if near wall meshes are good enough, often $y+$ is used, shown in the following equation 6

$$y+ = \frac{y u_\tau}{\nu} = \frac{y}{\nu}\sqrt{\frac{\tau_w}{\rho}} \tag{6}$$

with y being the distance between a wall and the mesh cell closest to the wall, ν being the kinematic viscosity, u_τ being friction velocity, τ_w being WSS and ρ being the density of the fluid. For proper resolving of near wall flows, usually the mesh is made such that $y+ \approx 1$ [56], which needs to be done by performing the simulation, checking the $y+$ values, refining the mesh if it is above $y+ \approx 1$ and repeating this procedure.

For highly turbulent flow, often wall functions are used instead of making a fine near-wall mesh in order to have a less computationally demanding mesh by allowing bigger cell sizes near a wall [57]. With standard wall functions the y+ value needs to be within $30 < y+ < 200$ (log-law region) [57], which allows for bigger cell sizes compared to $y+ = 1$ requirement, as the y from equation 6 (cell size near wall) can be bigger. Wall functions are empirical functions fitted to measured flow behaviour close to a wall [57].

2.2.3 Timestep

In CFD, it is generally advised the keep the Courant number below 1 [58], see the following equation 7

$$C = \frac{u\Delta t}{\Delta x} \tag{7}$$

with u being the velocity, Δt being the timestep size and Δx being the characteristic mesh cell size whose dimension is length. If the CFD Courant number is above 1, information from 1 cell can skip over multiple cells to reach the next cell, as the velocity in that cell is so high that with a timestep such that $C > 1$ the distance covered with that velocity would be greater than a single cell length. This can lead to solver instability and inaccuracy in the results.

2.2.4 Laminar and turbulence settings

To evaluate if a flow is turbulent, one generally looks at the Reynolds number, see the following equation 8

$$Re = \frac{\rho u D}{\mu} \tag{8}$$

with ρ the fluid density, u the flow speed, D a characteristic length scale (like aorta diameter) and μ the fluid viscosity. Generally speaking for steady pipe flow, turbulent flow can start to occur when the Reynolds number goes above 2000 [25, 59] and becomes fully turbulent at Reynolds numbers above 4000 [60]. For Reynolds numbers between 2300 and 4000, pipe flow is considered to be in a transitional regime [61] which is a mixture of laminar and turbulent flow. Within the aorta peak Reynolds numbers between 4000 and 10000 have been reported to occur with mean flow giving Reynolds numbers of around 1000-1200 [24]. Similar aorta CFD work often uses turbulent or transition flow modelling for Reynolds numbers above 2000 and laminar modelling if below 2000 [19, 24, 62, 26]. An example of a transition flow model is a model that switches between laminar and turbulence modelling based on the Reynolds number [62], which is used when modelling flow in the transitional regime as is often the case for aortic flow.

In aorta CFD work, various models for turbulent modelling are used, however often laminar modelling is used [26] and assumed because of the mean Reynolds number for aortic flow being rather low at $Re = 1350$ [40, 63]. As aorta wall degradation is partly caused by high WSS, and high WSS being related to higher velocities and turbulence from valve abnormalities, the use of turbulent modelling for CFD work with aTAA patients can be important. Similar work has shown that the usage of turbulence modelling for aorta CFD can be important, as a case with aortic valve stenosis was shown to have up to 40% of WSS being caused by turbulence [64].

Two models often used for turbulence in aortic CFD are: Large-eddy simulation (LES) [35, 64, 40] and $k-\omega$ Shear Stress Transport (SST) [19, 25, 40]. Work from Caballero et al. [40] on reviewing other CFD works in the thoracic aorta showed that out of 46 various works, 40 of them included laminar flow, 6 of them included SST turbulent flow and 2 of them included LES.

The transitional k-ω SST turbulence model has been found to predict WSS better compared to other RANS models [25], based on studies on coronary arteries. An analysis by Santos et al. [65] concluded that the k-ω SST model is more suitable for estimating WSS in the aorta compared to other RANS models.

For LES, it has been shown that laminar simulations with the same (fine) mesh and time-step value as a LES simulation can provide TAWSS results close to that of a LES simulation, with highest WSS difference being 5.1% [35]. Although the article did note that it did not see a benefit for running such a laminar simulation compared to LES based on computational cost.

2.3 Relevant previous works

In this section, works that are directly relevant to this study in terms of researching ascending aortic flow and the relation between inflow profile parameters and WSS are shown. The inflow profile is discussed in detail as it is an important part of this study.

2.3.1 Inflow profile

For both steady and unsteady flow simulations, work on aorta CFD often either use simplified inlets or parabolic inlet velocity profiles. In other cases they base inlet velocity profiles on measured data from patients, using techniques like phase contrast magnetic resonance imaging (PC-MRI) or 4D flow MRI [66, 67]. For unsteady work, the time-varying inlet condition is often based on patient-specific measured 4D flow data, measured flow or velocity waveform data of patients or generic (non-patient-specific) waveform data [66]. For steady work, often averaged flow over time is used, or systolic peak flow is used [19], as peak flow should have the biggest effect on WSS (higher velocity should generally mean higher velocity gradients near walls).

Pirola et al. [68] showed that neglecting secondary flow components of an inflow profile (using only the normal components against using all 3D velocity components) lead to an underestimation of the peak velocity by 19% (0.66 and 0.82 m/s) and of the mean velocity of 41% (0.16 and 0.27 m/s) at the inlet. This is also accompanied with differences in peak WSS values of 15% when comparing flat inlets to 3D inlets. It also notes that the usage of flat inlets could be sufficient for regions away from the thoracic aorta, which is not the case for this thesis.

Renner et al. [36] showed that flat inlet profiles are not good enough (compared to patient specific profiles) for WSS estimation, specifically in the aortic arch, with differences being at 8-34%. But it also showed that the WSS difference at systolic peak time was much lower, around 8%.

To compensate for the lack of patient-specific information on valvular velocity profiles in aTAA patients, Saitta et al. [69] produced a dataset of realistic 4D synthetic aortic inflow velocity profiles using statistical shape modelling. The dataset, which was used in this work, is accompanied by a list of variables that describe the shape of the inflow profiles. These variables are as follows: positive peak velocity (PPV), flow dispersion index (FDI), flow jet angle (FJA), secondary flow degree (SFD) and retrograde flow index (RFI). Table 3 provides short descriptions of these variables.

Label	Parameter description
PPV	Peak positive velocity at the inlet profile
FDI	Flow dispersion index: Ratio between area with top 15% of peak velocity magnitudes and the inlet area
FJA	Flow jet angle: Angle formed by the mean velocity direction and the unit vector orthogonal to the inlet surface
SFD	Secondary flow degree: Ratio between mean in-plane (radial) velocity magnitude and the mean axial velocity magnitude
RFI	Retrograde flow index: Fraction of negative area under the curve of the flow rate time-course over the whole area under the curve

Table 3: Table showing aorta inflow parameters and their descriptions [69]

2.3.2 4D Flow MRI and CFD

Studies that research flow within the ascending aorta often use 4D flow MRI [70, 71, 72, 73, 74, 75, 76, 77, 78]. This technique allows to acquire the in vivo 4D (3D and time) velocity fields. This data is usually gathered with a spatial resolution above 1 mm and a temporal resolution of around 40 ms.

Piatti et al. [79] showed that for ascending aortic flow from BAV-affected patients, the spatial resolutions ($\geq$1 mm) of 4D flow imaging were insufficient to accurately capture WSS. CFD simulations using 4D flow MRI allow a more accurate way of extracting WSS while still providing good agreement with in vivo flow conditions [80].

2.3.3 WSS relations in ascending aorta

Studies around ascending aortic flow mostly focused on the effect of bicuspid aortic valve disease on the flow features and WSS [71, 73, 75]. It has been shown that people with BAV disease can have elevated WSS, which significantly correlated with peak systolic velocity [71].

Hojin et al. [8] showed that for higher FJA there was significantly higher max WSS in the thoracic aorta and potentially lower impingement angles in the ascending aorta (figure 5 shows the impingement angle, α). The authors hypothesize that this happens in part because the flow with low FJA has a longer travel length until it hits an aortic wall, causing the jet to dissipate before it hits a wall. For flow with high FJA, the angle caused the jet to hit a wall earlier before the jet dissipated, causing impingement at higher velocity magnitude values compared to the low FJA jet. Hojin et al.'s study [8] used a 3D-printed patient specific aortic vascular phantom. With the print they tested jet inflow at angles of 0, 15 and 30 degrees in 4 different directions for 9 total different jet inflows tested. The tests used water at a Reynolds number of 5392 and only look at flow close to systole blood flow conditions. For capturing of results 4D PC-MRI was used with a spatial resolution of 1 mm and a temporal resolution of 73 ms.

Bissel et al. [81] showed that increasing FJA lead to more rotational flow and lower impingement angles, which was associated with an increase in WSS values.

Fillingham et al. [9] showed that for general (non-aorta) jet flow a lower impingement angle leads to lower maximum WSS values.

There is a contradiction between a lower impingement angle leading to lower WSS [9] and studies showing the opposite [81, 8]. This could be attributed to Fillingham et al. [9] doing controlled tests to show the effect of only the impingement angle changing (consistent travel length until wall impingement) and other studies testing aortic flow of different patients without controlling for the impingement angle [81] and at different inflow angles in the same aorta [8] leading to various jet travel lengths for the various inflow angles.

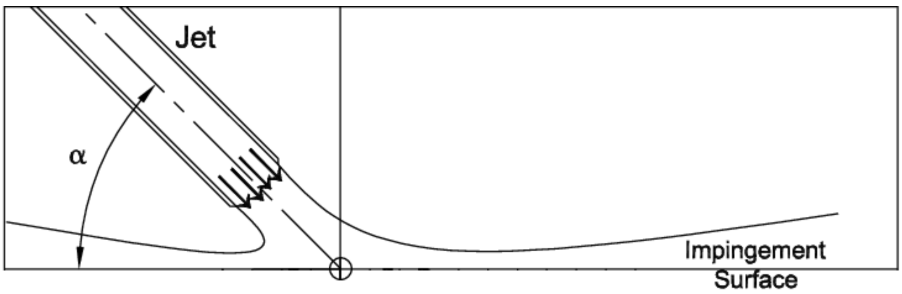

Figure 5: Visual description of impingement angle α [82]

3 Methodology

In this chapter the general methodology and automation steps for the transient simulations to find a possible relationship between FJA and WSS is described. The general workflow can be seen in figure 6 and consists of: making preliminary meshes, making the simulation meshes, preparing inflow profile data, producing Fluent cases and running the Fluent cases to generate WSS data.

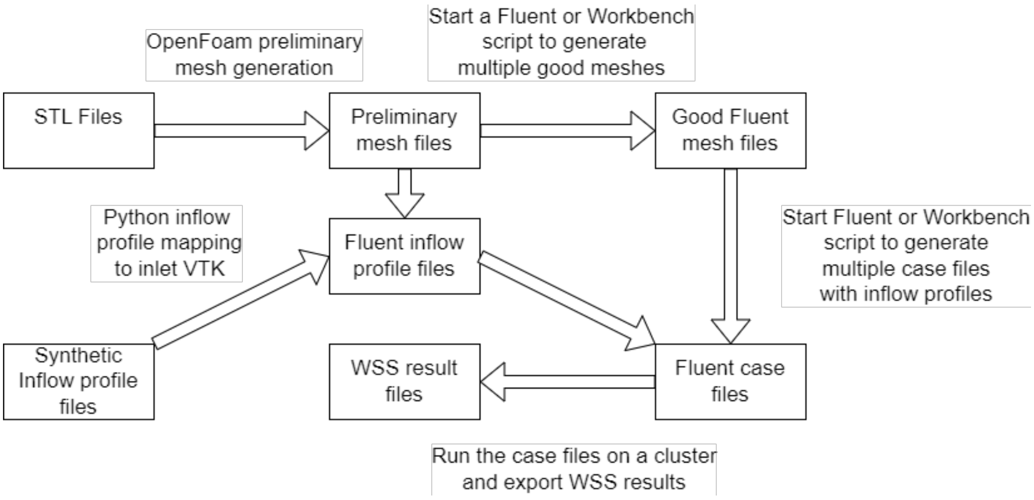

Figure 6: Chart showing the general workflow process

3.1 Geometry

The geometries used are aorta STL files from Romero et al. [15]. These geometries are simplified and do not contain any branches, they have only a single inlet and outlet. The aortic geometry starts near the aortic root in the ascending aorta up to the descending aorta, which is standard for most ascending aortic flow studies.

The geometrical data of the specific aortic geometry used in this study is shown in table 12. Information about the geometrical variables can be seen in table 1. The chosen geometry has ascending aorta phenotype E. This aortic geometry was randomly chosen from a synthetic aorta dataset[1] from Romero et al. [15]. The dataset contains 3000 different synthetic aortic geometries, consisting of separate STL files for the inlet, wall and outlet. An example of the aortic geometry can be seen in figure 7.

	PA	PD	PT	LPD	MA	SoV	k	h	w	h/w	tor
Chosen Geometry	15.35	11.41	12.58	226.49	18.73	14.03	7.49	84.53	68.35	1.24	0.70
Average	14.71	11.95	13.27	233.22	17.20	15.24	7.32	92.11	70.97	1.32	0.70
Max	20.24	16.44	18.26	329.19	24.53	22.83	8.81	146.67	111.64	2.39	0.78
Min	10.89	7.92	8.71	154.07	11.90	9.84	5.97	43.95	39.81	0.55	0.64
Standard Deviation	1.33	1.13	1.47	24.57	1.76	1.89	0.41	14.37	10.36	0.27	0.02
Median	14.61	11.89	13.21	230.83	17.11	15.11	7.31	90.78	70.39	1.31	0.70

Table 4: Table showing geometric variables of the chosen aortic geometry and data about the entire aortic geometry dataset [15]. A description of geometric variables is found in table 1 and figure 3

[1]This dataset is publicly available, but the hyperlink in the cited article [15] does not work anymore, the new website can be found in this hyperlink: https://www.uv.es/commlab/repository.html

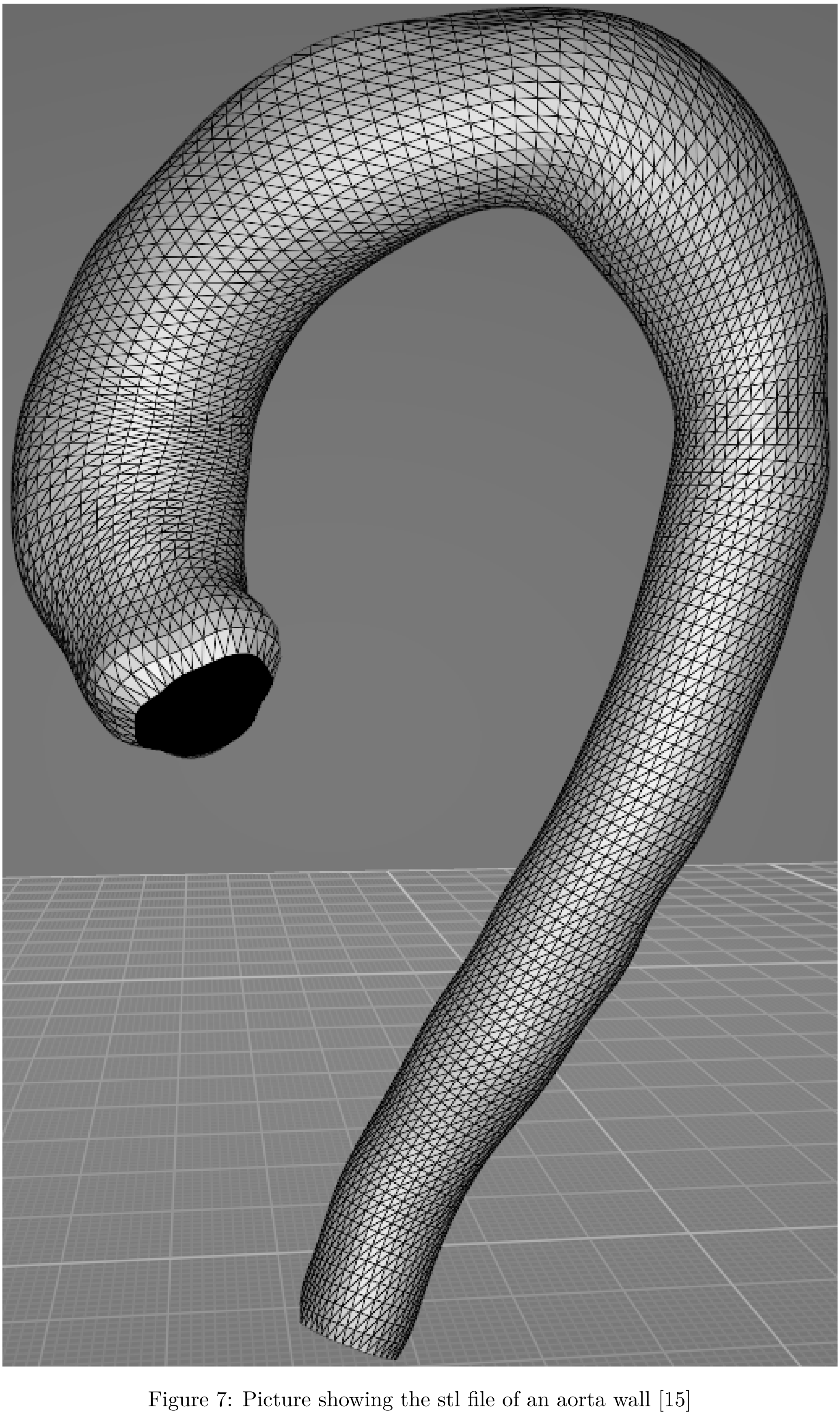

Figure 7: Picture showing the stl file of an aorta wall [15]

3.2 Mesh

In order to produce meshes automatically in Fluent for a number of geometries or inflow profiles, a preliminary mesh must be made.

3.2.1 Preliminary mesh

CFmesh (part of OpenFoam) is used to create meshes of various aortic geometries. These meshes are used for importing into Fluent meshing. This preliminary mesh step is needed to automate Fluent mesh generation from STL files, because Fluent meshing does not directly accept STL files. This preliminary mesh step is easily automated in OpenFoam and Fluent easily accepts this preliminary mesh for its own mesh generation while recognizing the inlet, outlet and wall boundaries. The shell script file and meshDict file for cfMesh can be found in appendix A, where they show the code for making meshes from six different aortic geometries.

The meshDict file is used to input in cfMesh the information needed to create the meshes. The important part is the additionalRefinementLevels within the localRefinement section, where the aortic wall and inlet are given more mesh refinment to ensure the mesh properly captures the features of the STL geometry files.

The shell script file takes prepared STL geometry files of an inlet, an outlet and a wall, and combines them into a single STL file while retaining the three different patches. Then it creates a surface FMS file (OpenFoam proprietary file format used to describe different patches in a single file) which is used by cfMesh and the meshDict file to create a mesh. The mesh is scaled to get the right units in Fluent and checked for quality which is recorded in the file 'MeshCheck.txt'. Afterwards the mesh conversion to a Fluent format is done, which is the most time consuming part of the process. Finally, the inlet mesh is saved as a VTP file (Visualization Toolkit Polygonal Data, used for storing VTK surface models) for later in the inflow profile mapping process.

3.2.2 Simulation mesh

To automate the mesh production process for multiple geometries, Ansys Workbench scripting was used. This worked by generating a mesh manually with all necessary settings, while Workbench scripting recorded all actions taken in the Fluent meshing process. Workbench saved the actions taken to a script file. This script file was edited with a for loop to perform the same actions, but with alterations each loop to import different geometries or inflow profiles and export a case or mesh under a different name. The script file could be run by Workbench to perform all actions within the script, including any alterations made. An example code can be seen in Appendix B. This example shows the importing of a geometry, importing of an inflow profile, mesh generation, case preparation, case export and a for loop that takes the same actions but changes the imported geometry and exported case file name each loop.

The mesh used for the final simulations is generated using Fluent. The settings used for making this mesh in Fluent are: Polyhedral mesh, 10 smooth transition inflation layers with a growth rate of 1.2 on the aortic wall, max cell length of 0.42 mm and general growth rate of 1.2, and initial surface mesh generation with minimum size of 0.19 mm, maximum size of 4.9 mm and growth rate of 1.2. This results in a mesh with around 5 million cells. The mesh is analysed in section 3.5.

A polyhedral mesh is generally better in approximating gradients and generally leads to a more accurate solution with less cells compared to tetrahedral meshes [83].

3.3 Solver settings

The solver settings used in Fluent are as follows: SIMPLE scheme, Rhie-Chow distance based Flux type, Least Squares Cell Based gradient, Second Order pressure spatial discretization, Second Order Upwind momentum spatial discretization, Pseudo Time Method turned off, First Order Implicit transient formulation, Warped-Face Gradient Correction turned on, transient with 0.001 s timestep, Fluent absolute convergence criteria for residuals at 10^{-3}, laminar flow, rigid walls, incompressible fluid, Newtonian viscosity at 3.5 mPa·s, blood density at 1000 kg/m^3 and Under-Relaxation factors for pressure, density, body forces and momentum at 0.3, 1, 1, 0.7 respectively.

The chosen solver settings are mainly based on the following: preliminary testing on trying to get steady state simulations to work for one of the inflow velocity profiles, preliminary testing of optimizing transient simulations for the inflow velocity profiles, advice from my supervisors and conditions that are generally used in other aortic CFD work.

For the final simulations, transient simulations are used instead of steady simulations, even though the inflow profiles do not change in time. This is done because testing showed that steady state simulations were unable to converge, likely because of the tested flow showing transient behaviour in the tested transient simulations. This testing was done with a mean systolic peak inflow profile from the used inflow profile dataset [69], see section 3.4.1.

The SIMPLE scheme is used instead of the PISO scheme for the final simulations, even though PISO is generally recommended for transient simulations. This is done because of the relatively high time step used with a maximum Courant number of 5 occurring in the flow, see section 3.5. The PISO scheme can become unstable for large timesteps and if a lot of iterations (more than three) are needed for every timestep [84]. The higher stability of the SIMPLE scheme at larger timesteps is the reason it was chosen.

3.4 Boundary and other conditions

The most important boundary condition is the velocity at the inlet. The inlet is set to use different inflow velocity profiles from Saitta et al. [69], explained in section 3.4.1. Other (boundary) conditions are noted in section 3.4.2.

3.4.1 Inflow profile

The data used for the inflow velocity profiles comes from a dataset from Saitta et al. [69]. This is a dataset of 437 various synthetic inflow velocity profiles, generated with principal component analysis and statistical shape modelling using 4D flow MRI scans of 30 subjects with ATAA. These velocity profiles contain data across the cardiac cycle, but only data at systolic peak (chosen as time in cardiac cycle with highest positive peak velocity, which can differ by about 5% of time of a cardiac cycle) was considered. This is done to simplify the problem and focus on the effect systolic peak flow has on WSS.

The parameters used to characterize the inflow profiles from Saitta et al. [69] are: positive peak velocity (PPV), flow dispersion index (FDI), flow jet angle (FJA), secondary flow degree (SFD) and retrograde flow index (RFI). Descriptions of the parameters are shown in table 3 from section 2.3.1. The dataset is accompanied with Python codes to map these inflow profiles to any inlet shape. Two examples showing the inflow profile shape at systolic peak flow from Saitta et al. [69] can be seen in figure 8, where red shows the maximum velocity magnitude on the profile.

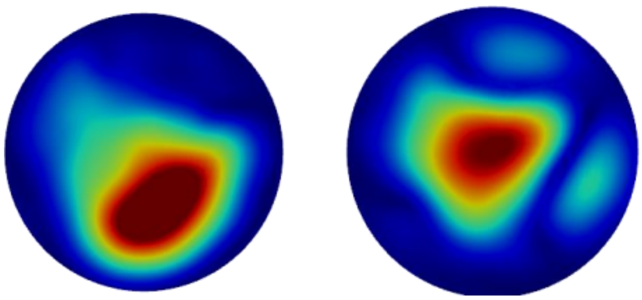

Figure 8: Examples of inlet velocity profiles [69]

In this study, the effect of the FJA on WSS is investigated. For this, the original inflow profile dataset is filtered to find profiles with a small range of values for FDI and PPV. SFD and RFI are not considered as SFD and FJA are related to each other and RFI is a time based variable, which is irrelevant if only using systolic peak velocity profiles. After filtering of the dataset, 20 velocity profiles are chosen that have a core jet FJA (CJ-FJA) of each profile between 8 and 26.5 degrees. The CJ-FJA is here defined as the FJA using only 10% of the inflow profile area with the highest velocity magnitudes. The CJ-FJA and total FJA values for the chosen profiles can be found in appendix D. The CJ-FJA is used because it is thought that for peak WSS the FJA of the high velocity jet part of the inflow profile is more relevant than the FJA of the entire inflow profile.

The FJA is the angle between the normal vector of the inlet surface (the blue vector in figure 9) and the mean velocity vector of an inlet velocity profile (the red vector in figure 9). Different inlet velocity profiles can have different FJA values. The direction of the mean velocity vector can also change by rotating along the normal vector without altering the FJA. This other change of direction is defined by the secondary angle. The secondary angle is the angle between two different mean velocity vectors of two different inlet velocity profiles, with the angle being along the normal vector as the axis of rotation. Figure 9 shows a secondary angle of 90 degrees between the red mean velocity vector and the different green mean velocity vector. For the 20 chosen velocity profiles, the secondary angle of the first velocity profile is set at zero degrees. The secondary angles of the other velocity profiles is relative to the first profile. The range between the profile with the lowest secondary angle and the highest secondary angle is 90 degrees.

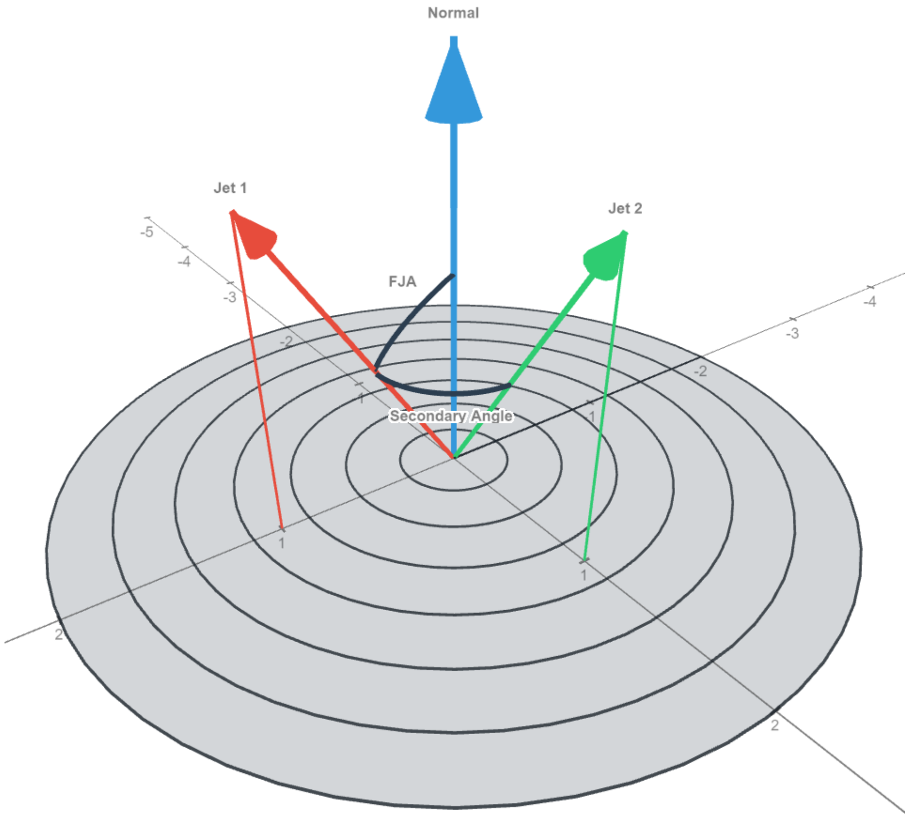

Figure 9: Visual description of FJA and secondary angle made with Math3d [85]

The python code from Saitta et al. [69] is used to map the chosen synthetic aortic inflow profiles to the inlet VTP files from the OpenFoam mesh generation. Appendix C shows the parts of the code responsible for mapping the profile and for converting them into a Fluent format. The code is adjusted from the source, so that multiple Fluent inflow profiles are created from multiple synthetic inflow profiles, with a single aortic inlet.

The mapping code uses 20 different synthetic inflow profiles and a single aortic inlet VTP file. It maps the 20 circular inflow profiles unto the specific shape of the aortic inlet and gives a VTP file for each of the 20 inflow profiles. It uses sections of 'utils.py', which can be found on the GitHub from Saitta et al. [69].

The Fluent format conversion code takes the 20 mapped inflow profiles and converts them into velocity profile files accepted by Fluent.

3.4.2 Other boundary conditions

Other boundary conditions that are used are a zero pressure outlet and a no slip condition at the walls.

Regarding the outlet condition, for aortic flow with multiple outlets, work from Pirola et al. [86] has shown that a three-element Windkessel model at all outlets has the best performance and that simple zero pressure outlets do not perform well. However, for aorta flow models with only a single outlet, a zero pressure should be good enough, as flow towards other branches is of less importance, and the area of importance (ascending aorta) is relatively far from the outlet, decreasing its effect on flow in that area, as the inlet condition should have a bigger impact on flow there. There is no source directly saying a zero pressure outlet is good enough for a single outlet model, but there is a source saying that zero pressure outlet becomes a problem when it is used at multiple outlets [40] and a source simulating aortic flow with a single outlet and using a zero pressure outlet [87].

Other outlet conditions often used in CFD aorta work are based on patient specific flow parameter measurements and are directly used at the outlet [40]. This is not of much importance for this study, as such patient specific measurements are impossible to do for synthetic aortic geometries and each simulation only has a single outlet.

3.5 Mesh and timestep analysis

To determine if a generated mesh is accurate enough, multiples meshes are simulated in Fluent with the mean aortic inflow velocity profile from Saitta et al. [69] at systolic peak velocity while looking at the WSS results averaged between the time the aortic jet hits a wall and end time of the simulations. For this, three meshes are used with data as in table 5. As the percentage difference for (99^{th} percentile WSS) was below 3% when comparing the 5 and 11 million cell meshes, the 5 million cell mesh was chosen for the final simulations.

To determine the timestep, simulations were performed similar to the mesh analysis, but with varying timesteps ranging from 0.01 to 0.0001 s, as in table 5. A timestep of 0.001 s with a corresponding maximum Courant number of 5 was deemed sufficient while still allowing the final simulation to be done in a reasonable amount of time. The reason for this timestep analysis being done is unusual WSS behaviour at high timesteps (0.1 - 0.01 s) and Courant numbers.

Max cell length in mm	1	0.42	0.3
Amount of cells in mesh in millions	2.5	5	11
99^{th} percentile WSS % difference	-	-5.2	0.5
Timestep in seconds	0.01	0.001	0.0001
Maximum Courant number	∼50	∼5	∼0.5

Table 5: Data for mesh and timestep analysis

The quality of the inflation layers is good enough, as the velocity profiles near the wall are accurately captured by the inflation layers, see $y+ < 1$ in figure 12, inflation layers in figure 11 and velocity throughout inflation layers in figure 10.

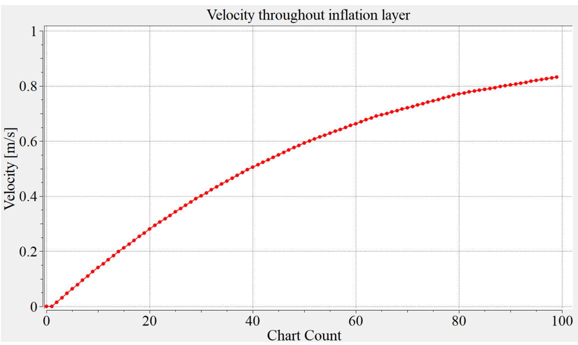

Figure 10: Picture of velocity throughout inflation layers

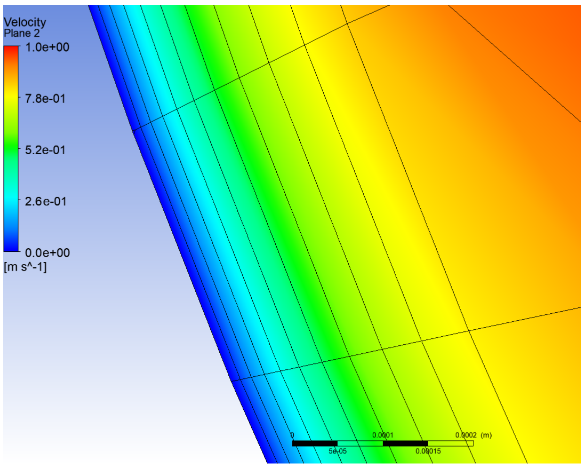

Figure 11: Picture of inflation layers

3.6 Final simulations

To prepare 20 Fluent cases for the final simulations, the same kind of Ansys Workbench scripting from section 3.2.2 is used. All the necessary steps to prepare a single case are manually taken, including setting the Fluent case such that it will export WSS data every 0.005 s over a total time of approximately 2.4 seconds, applying the proper inflow profile and exporting a case file. Workbench scripting repeats the process for the other 19 cases that need to be prepared.

Each case is run on the Process & Energy cluster for a single day. Each case has a different total simulation time, ranging from 2.37 s to 2.8 s. The lowest final time across the cases is taken as the end of the time range used to compare WSS data between the cases. The case files are run on the cluster using a Fluent journal file,

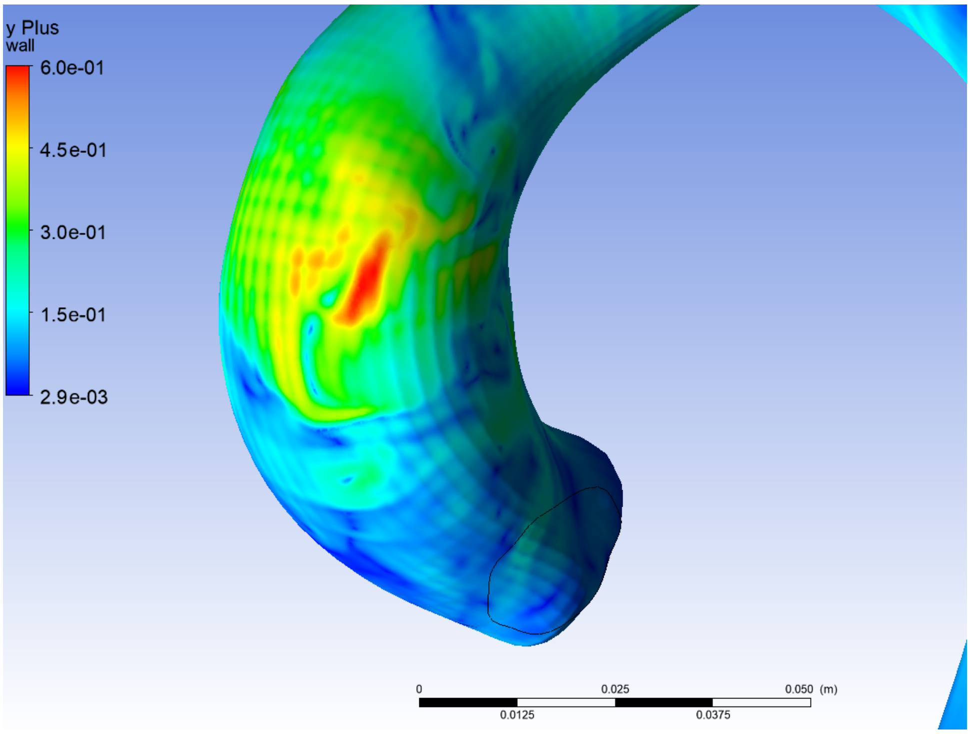

Figure 12: Picture of y plus across aortic wall

with Appendix B showing an example. The journal file initialises the system, sets the timestep and starts the solving process for a number of timesteps and maximum number of iterations for each timestep.

3.7 Post-processing

For correlating the WSS data with velocity profile variables, the average WSS across timesteps between 0.3 and 2.37 seconds is computed, and from that the 99th percentile of WSS across the ascending aorta area is taken for regression analysis. This starting time point is chosen as the approximate moment the jet flow from all inflow profiles should have hit a wall and the ending time point is based on how far 24 hours of computing could take the simulations. In this time range, the flow shows repeating transient behaviour with no sign of becoming steady. The 99th percentile WSS of inflow profile 77 from Appendix D across time is shown in figure 13, from which transient behaviour is clearly seen.

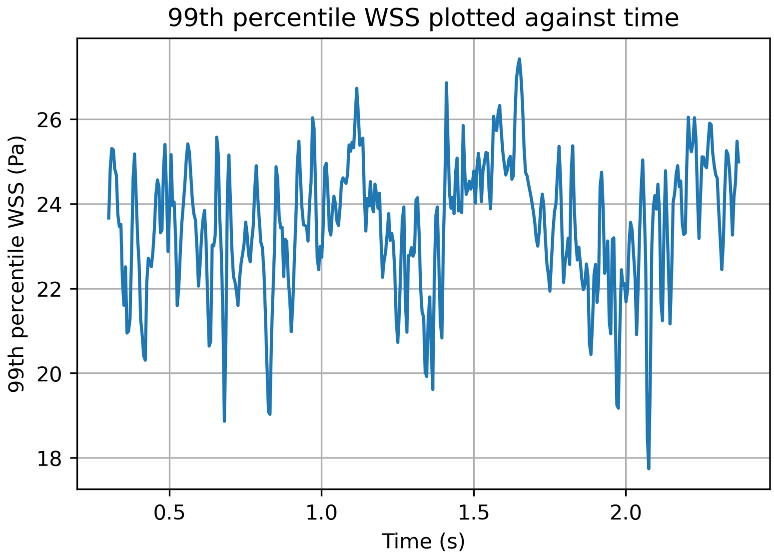

Figure 13: 99th percentile WSS across time

The variables that are investigated during post-processing are: FJA, eccentricity, flow rate, and the secondary inflow angle. The FJA is the angle between the normal vector of the inlet surface and the mean velocity vector of an inlet velocity profile. The eccentricity is how far the velocity magnitude weighted center of the inflow profile is located away from the geometric center of the inflow profile. The flow rate is the volumetric flow rate in m^3/s. The secondary inflow angle is the relative angle difference between the average velocity vectors of the inflow profiles when that vector is projected unto the 2D plane of the aortic inlet, as seen in figure 9. These inflow variables have respective ranges of 8 to 26.5 degrees, 0.55 to 2.3 mm, 0.13 to 0.24 L/s and total range of 90 degrees relative to the secondary inflow angle of the first inflow profile.

All inflow variables and WSS results, in the form of percentile values across the ascending aorta, are post-processed with linear regression modelling using Excel. The Significance level for regression modelling was set at $p < 0.05$. Other figures showing graphs, WSS data, flow streamlines and other post-processed figures are made with Excel, ParaView and Ansys CFD-Post.

3.8 Computational workflow time

The preliminary mesh creation takes about 15 to 20 minutes for a single aortic geometry on an i7-9700KF CPU without using the parallelization options in OpenFoam, so only a single core is used.

The creation of meshes and Fluent cases for the final simulations takes about 6-7 minutes for a single aortic geometry, with most time spent on the meshing process, which generates a mesh of approximately 5 million polyhedral cells. This is with using parallel processing with four cores.

The python code for generating inflow profiles takes about 1 minute per profile mapping and the Fluent conversion code takes less than 1 minutes for 20 profiles. The mapping seems to allow full parallelization using all six cores.

As an example, the generation of 100 cases with different aortic geometry would take about 29 hours of preliminary mesh creation and about 11 hours of Fluent mesh and case creation with an i7-9700KF CPU. Both of these need no user input while they are running, only needing user input for setting them up.

4 Results

In this section, the results regarding linear regression modelling of various inflow variables with WSS will be shown, together with some visualisation of the WSS and flow results. Results are discussed in section 5.

4.1 3D Streamlines

In figures 14, 15, 16 and 17 3D streamline comparisons at different viewpoints are shown between a low core jet FJA (CJ-FJA) inflow profile (profile number 77 from Appendix D) and a high CJ-FJA inflow profile (profile number 205 from Appendix D). These profiles have respective CJ-FJA values of 10.9 and 25.9 degrees, and are randomly chosen among profiles with a low CJ-FJA and profiles with a high CJ-FJA. The minimum CJ-FJA among the profiles is 8 degrees and the maximum is 26.5. The CJ-FJA is here defined as the FJA using only 10% of the inflow profile area with the highest velocity magnitudes.

In the figures the approximate area where the jet flow impacts the ascending aortic walls can be seen. Comparing this to the high WSS areas from section 4.4 shows that the area where the jet flow from the low CJ-FJA profile hits the aortic wall is the same approximate area of high WSS. For the high CJ-FJA profile the exact area where the jet hits the wall is harder to see, but comparing it with the WSS figures from section 4.4, it seems the area is more spread out than the low CJ-FJA profile.

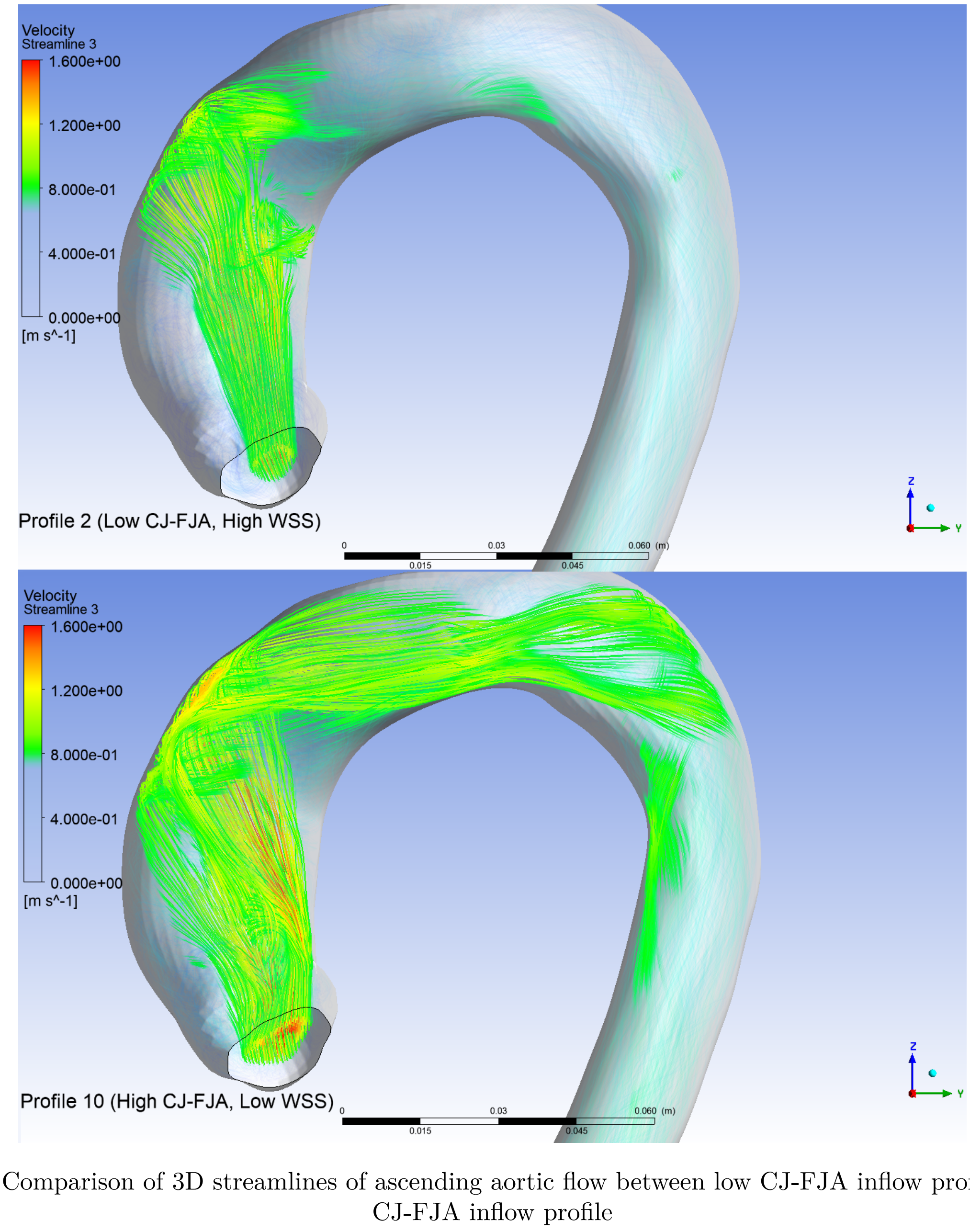

Figure 14: Comparison of 3D streamlines of ascending aortic flow between low CJ-FJA inflow profile and high CJ-FJA inflow profile

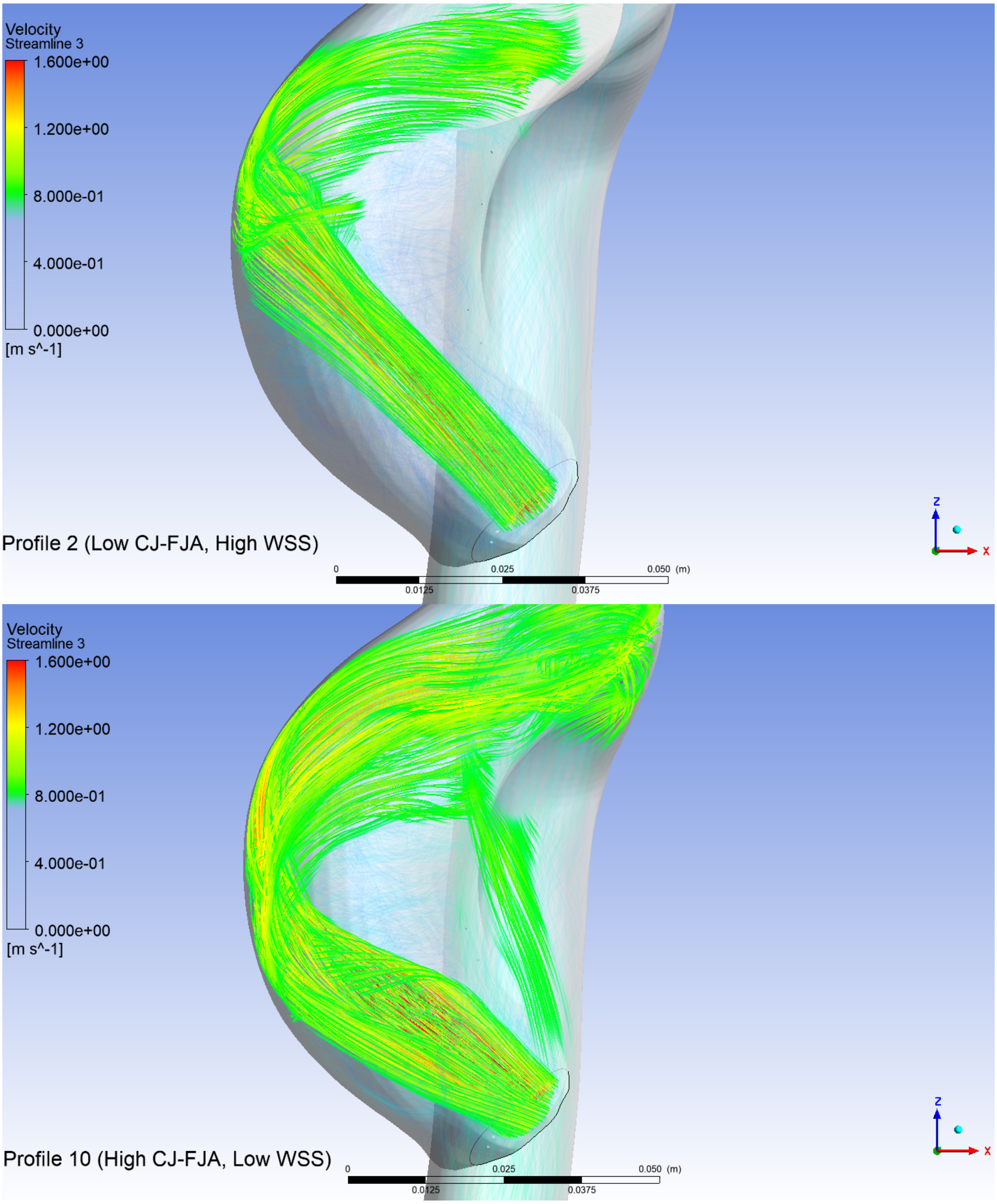

Figure 15: Comparison of 3D streamlines of ascending aortic flow between low CJ-FJA inflow profile and high CJ-FJA inflow profile. Viewpoint is rotated 90 degrees along the z-axis from figure 14

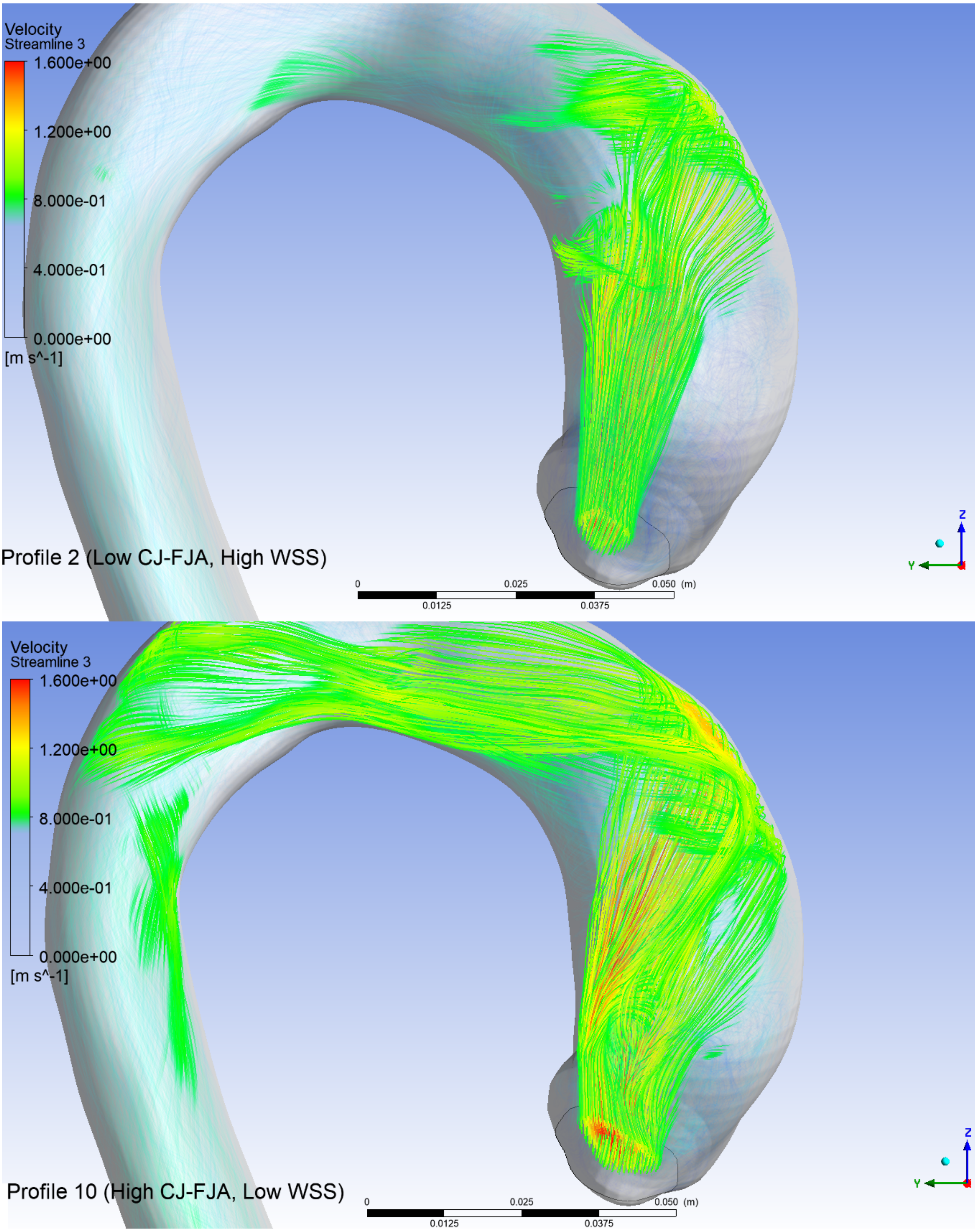

Figure 16: Comparison of 3D streamlines of ascending aortic flow between low CJ-FJA inflow profile and high CJ-FJA inflow profile. Viewpoint is rotated 90 degrees along the z-axis from figure 15

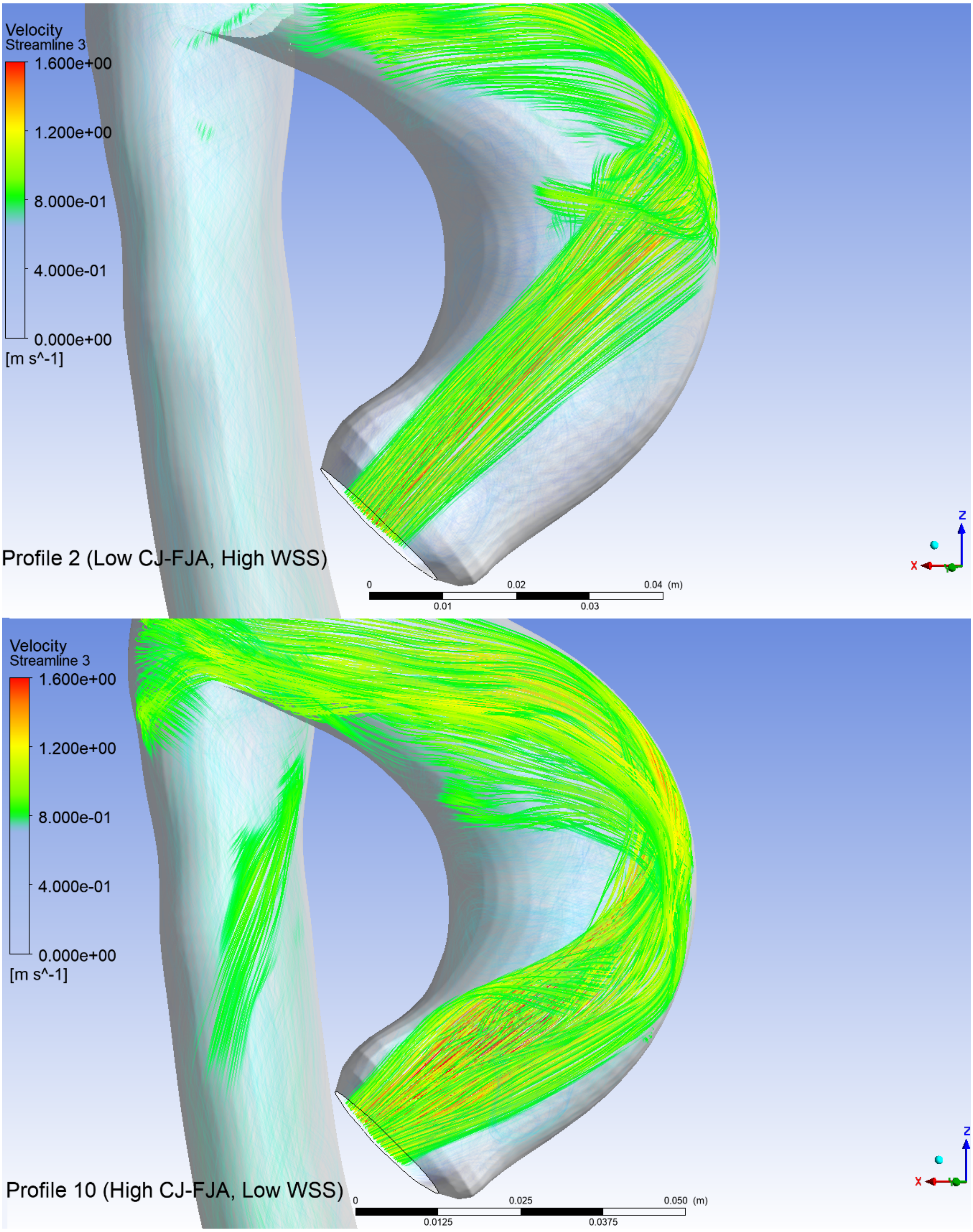

Figure 17: Comparison of 3D streamlines of ascending aortic flow between low CJ-FJA inflow profile and high CJ-FJA inflow profile. Viewpoint is rotated approximately 90 degrees along the z-axis from figure 16

Some additional 3D streamlines of profile number 436 from Appendix D at multiple viewpoints are shown in figures 18, 19, 20 and 21. This profile has a high secondary flow angle relative to the low CJ-FJA profile shown before. The figures show that the flow still hits the ascending aortic wall in a location similar to the previous 2 shown profiles.

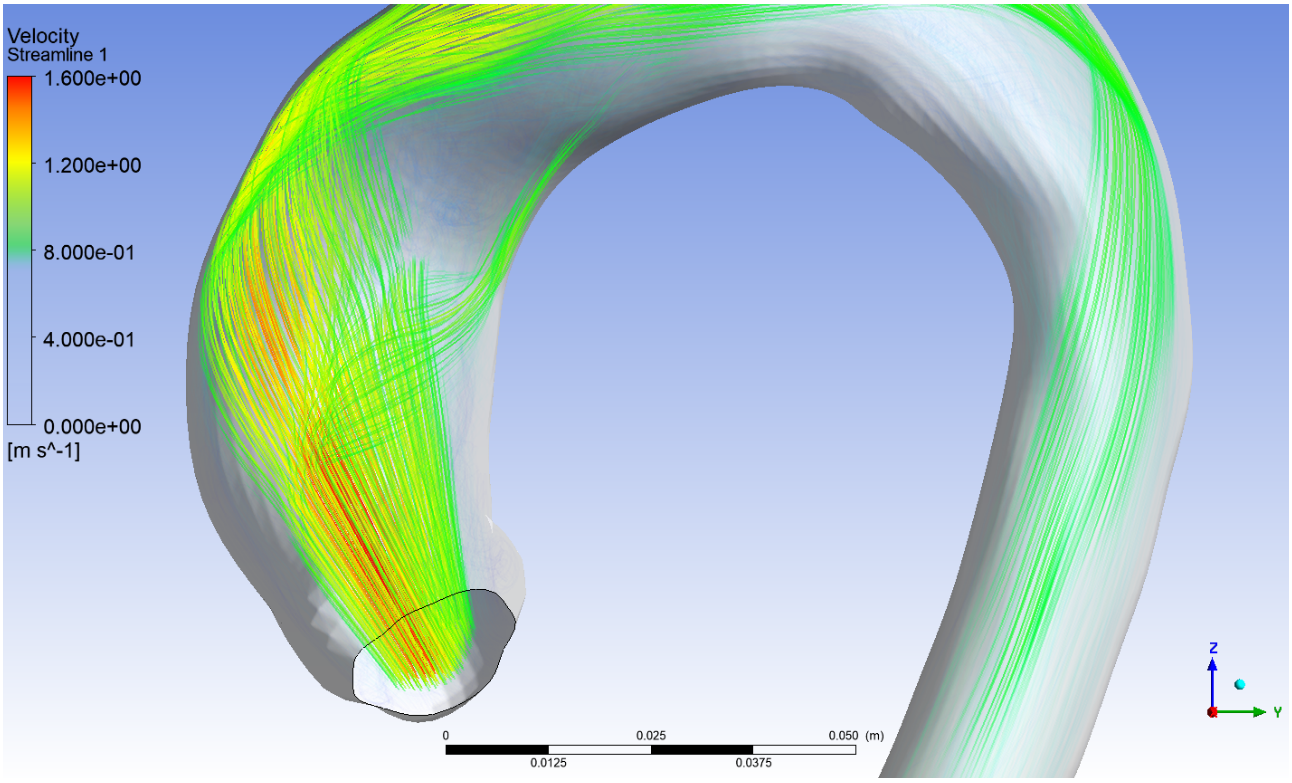

Figure 18: 3D streamlines of ascending aortic flow for a profile with a high secondary angle

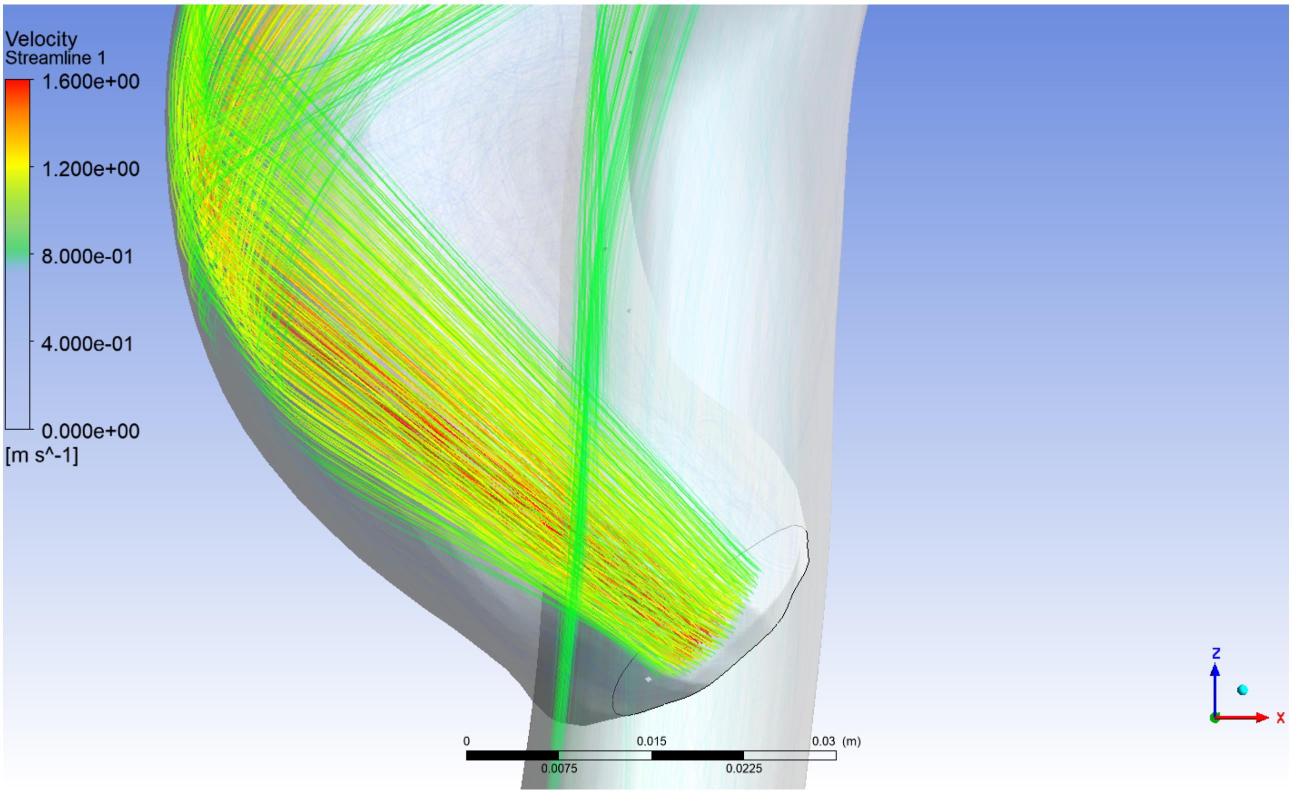

Figure 19: 3D streamlines of ascending aortic flow for a profile with a high secondary angle. Viewpoint is rotated 90 degrees along the z-axis from figure 18

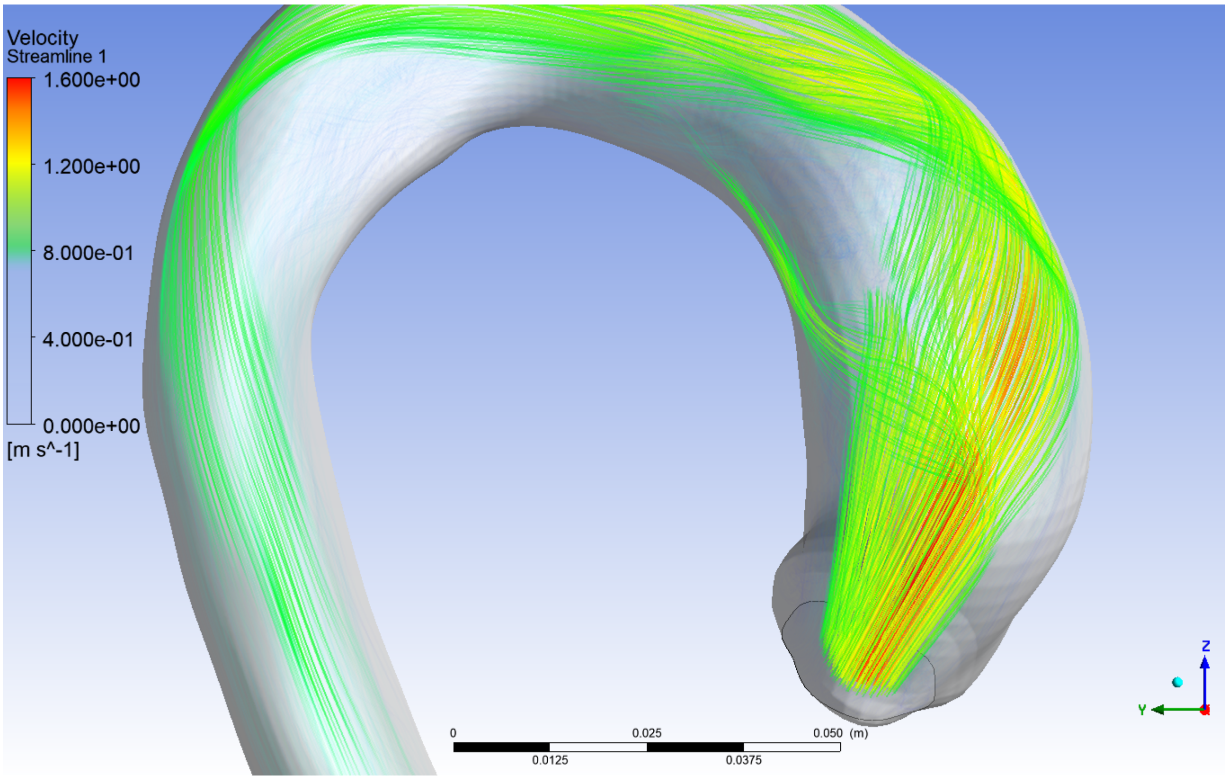

Figure 20: 3D streamlines of ascending aortic flow for a profile with a high secondary angle. Viewpoint is rotated 90 degrees along the z-axis from figure 19

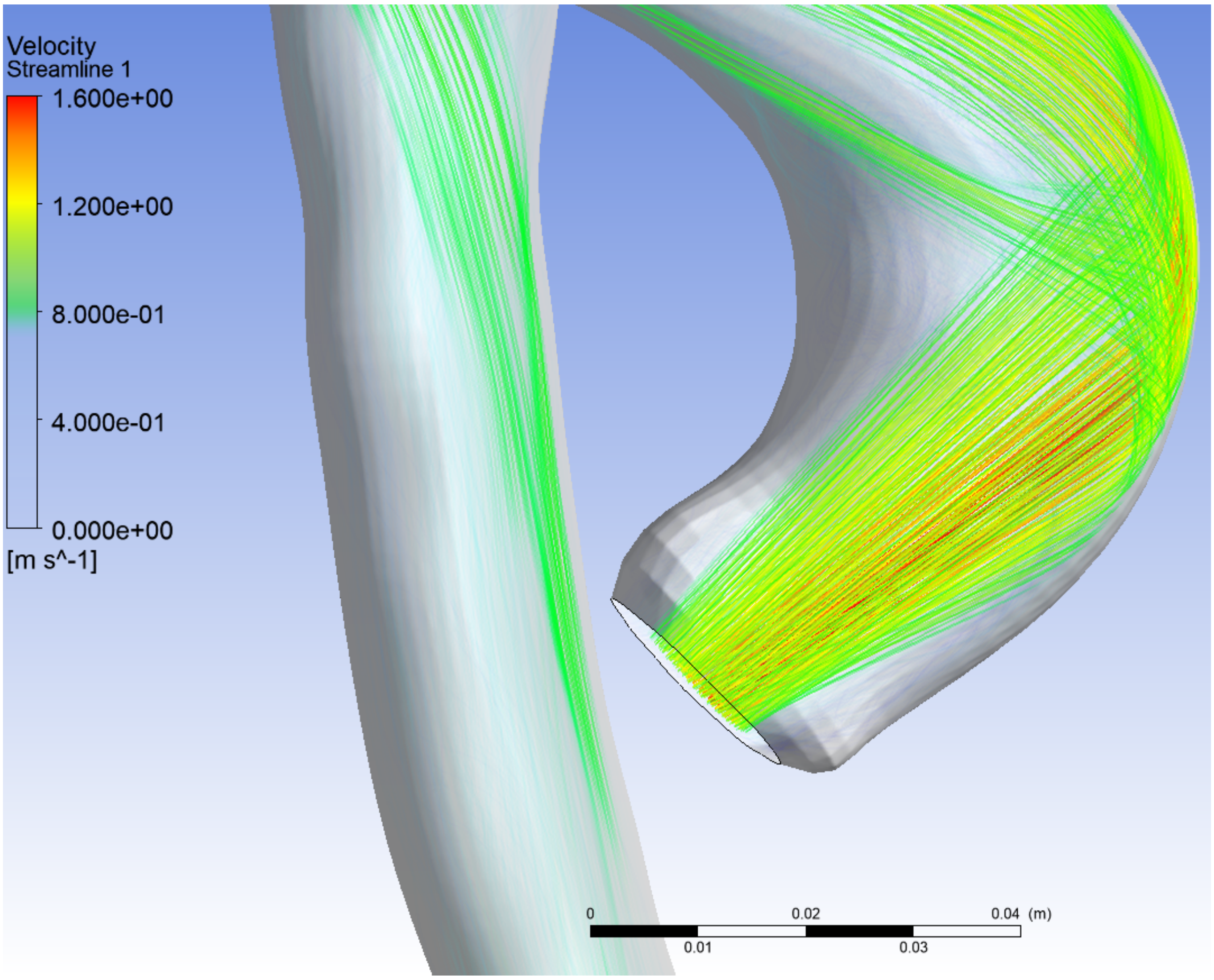

Figure 21: 3D streamlines of ascending aortic flow for a profile with a high secondary angle. Viewpoint is rotated approximately 90 degrees along the z-axis from figure 20

4.2 2D Streamlines

In figures 22 and 23 comparisons of 2D flow streamlines within the ascending aorta can be seen for low and high CJ-FJA profiles from section 4.1. The 2 different 2D cuts are perpendicular to each other. For the low CJ-FJA profile the 2D cuts show the jet hitting the wall at a high impingement angle. For the high CJ-FJA, using a 2D cut does not capture the flow well, but from figure 22 it looks like the flow hits the wall at a lower impingement angle as compared to the low CJ-FJA profile. Exact values for the impingement angles are not calculated in this study.

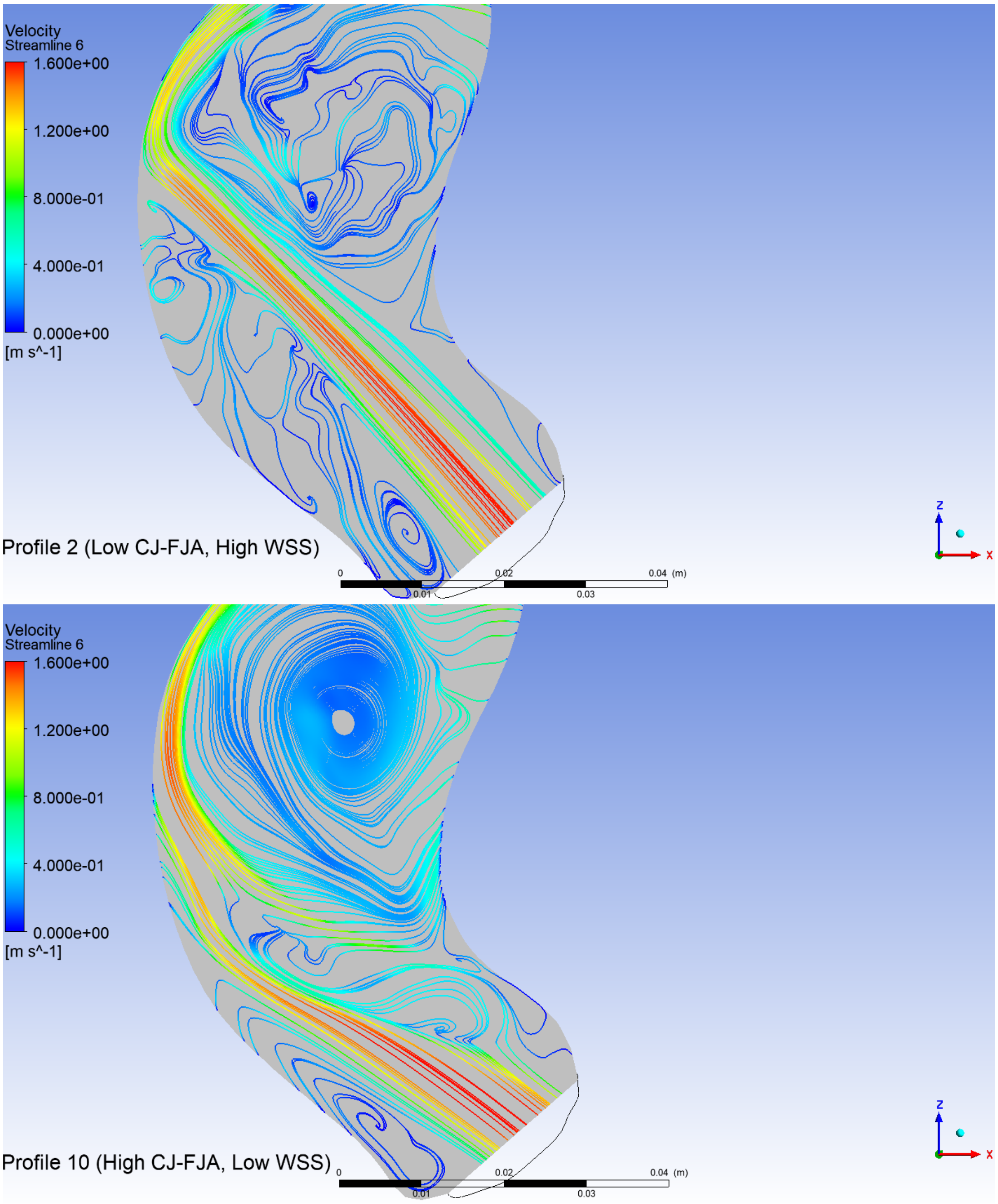

Figure 22: Comparison of 2D streamlines of ascending aortic flow between low CJ-FJA inflow profile and high CJ-FJA inflow profile

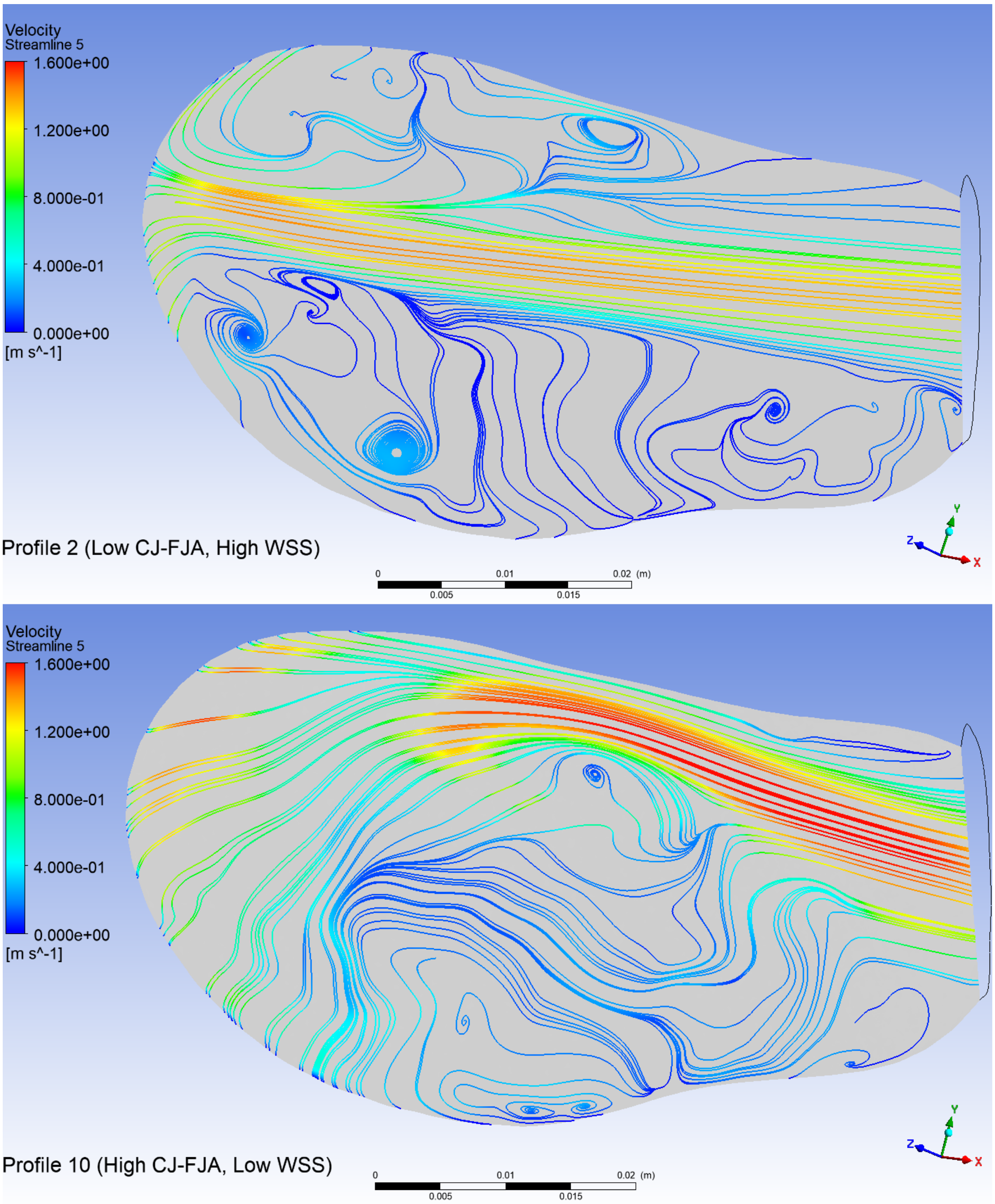

Figure 23: Comparison of 2D streamlines of ascending aortic flow between low CJ-FJA inflow profile and high CJ-FJA inflow profile. Perpendicular 2D cut to figure 22

4.3 3D Streamlines core jet

Figure 24 shows a 3D streamline comparison of the core jet flow for the same low and high CJ-FJA profiles as earlier sections. In this figure the impingement angle of the low CJ-FJA profile seems to be slightly higher than the high CJ-FJA profile based on approximate crude drawing of the impingement angles, see figure 25. If you take into account the bending of the jet from the high CJ-FJA profile before it hits the aortic wall, see figure 24, the impingement would be lower than shown in figure 25 and the impingement angle difference between the low and high CJ-FJA profiles would be higher.

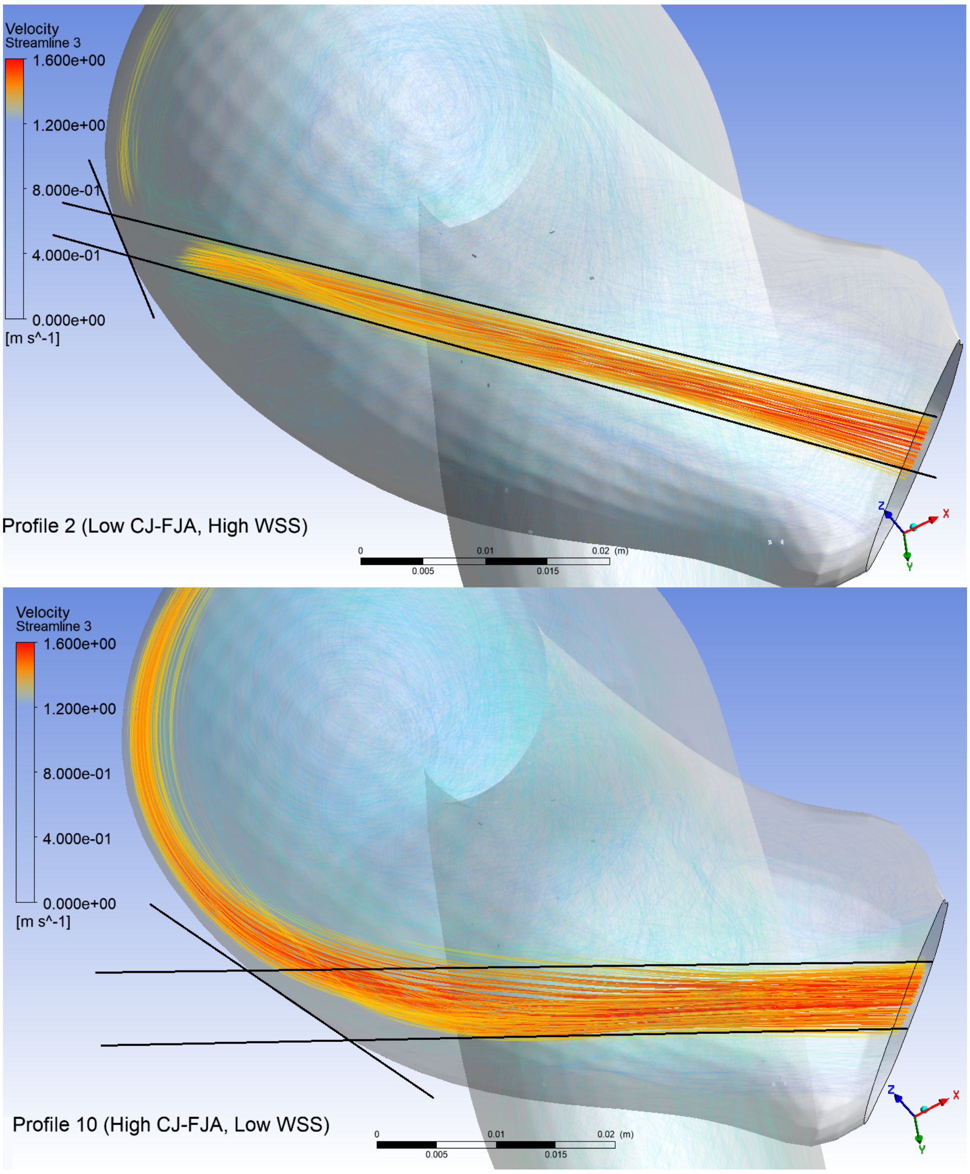

Figure 24: Comparison of core jet 3D streamlines of ascending aortic flow between low CJ-FJA inflow profile and high CJ-FJA inflow profile

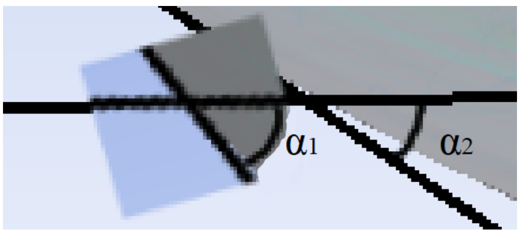

Figure 25: Left: Impingement angle α_1 of the low CJ-FJA profile. Right: Impingement angle α_2 of the high CJ-FJA profile. Shown angles come from the drawn angles in figure 24

4.4 WSS results

The WSS results used are averaged across the transient simulation time-spans. From this, the top percentile values in the ascending aorta, 90th to 99th percentile in particular, are looked at for further linear regression modelling. This is done to limit the effect of local mesh quality issues on the extracted results. The full WSS percentile results and the inflow variables for each profile can be seen in Appendix D

In figures 26 and 27 the WSS results are visualised for the same low and high CJ-FJA profiles as in the previous sections.

In figure 26, it can be seen that for the higher CJ-FJA profile there is generally higher WSS within the aortic arch. An elevated WSS spot near the ascending aortic inlet can also be seen for the higher CJ-FJA profile, which is caused by the jet flowing near the wall for flow caused by this specific profile.

On the bottom 2 visualizations of figure 26, the high peak WSS in the ascending aorta of the low CJ-FJA profile is clearly seen when compared to the high CJ-FJA profile. It can also be seen that within the general ascending aorta area, the high CJ-FJA profile has a larger area with elevated WSS (non-blue colour, above 2-4 Pa) compared to the low CJ-FJA profile. The same is seen for the aortic arch.

In figure 27 the areas with WSS above the 98^{th} percentile are visualised. From this it is clearly visible that the peak WSS occurs at the back of the ascending aorta, the location where the jet hits the aortic wall. The lower CJ-FJA profile presents a higher peak (98^{th} percentile) WSS compared to the high CJ-FJA profile.

At the bottom of figure 27 the high CJ-FJA WSS visualization is zoomed in. It is visible that an elevated WSS area near the ascending aortic inlet is included in the area above 98^{th} percentile WSS.

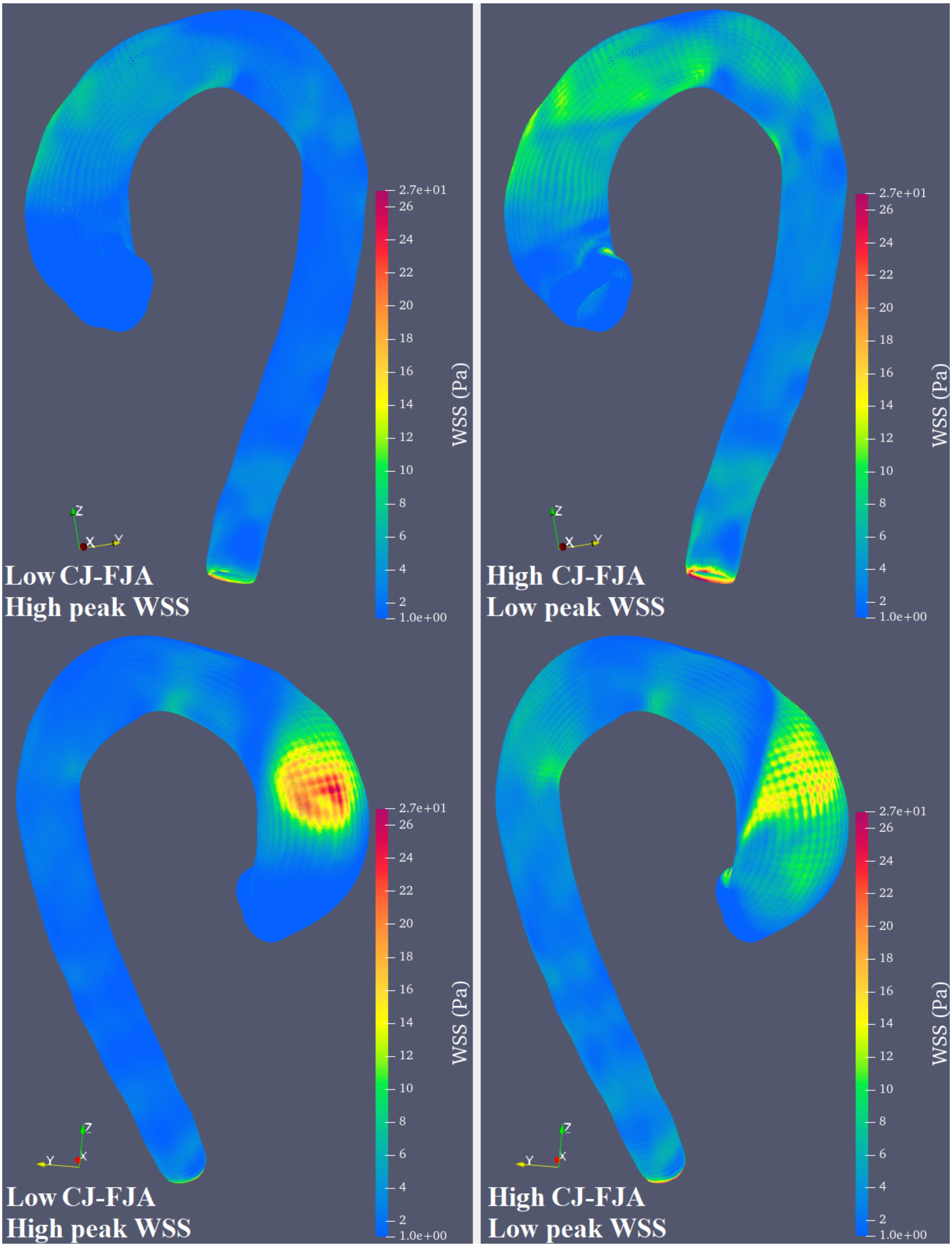

Figure 26: WSS results visualised for a low CJ-FJA profile and a high CJ-FJA profile

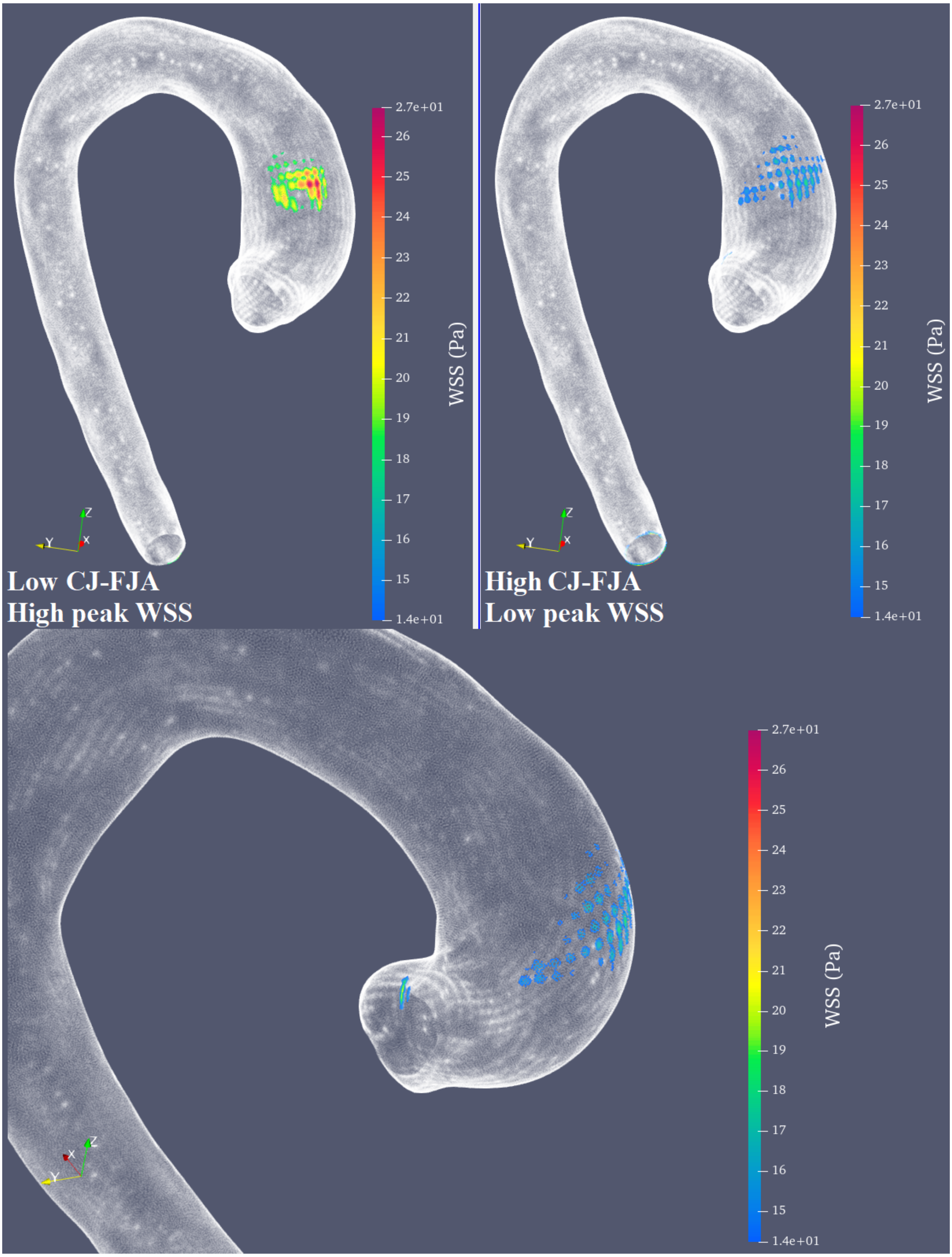

Figure 27: Top: Area above 98^{th} percentile WSS results visualised for a profile with low CJ-FJA and a profile with high CJ-FJA on the back of the aorta.
Bottom: Zoomed in visualisation of area above 98^{th} percentile WSS for the profile with high CJ-FJA

4.5 Linear regression modelling

The linear regression has been done with Excel using the Analysis ToolPak. The inflow variables used with linear regression modelling with various WSS percentile values are: CJ-FJA, FJA, the secondary inflow angle, flow rate and eccentricity.

4.5.1 CJ-FJA

The CJ-FJA, flow jet angle of 10% of the inflow area with highest velocity magnitude, has been shown to have a significant ($p < 0.05$) negative correlation with the 98$^{\text{th}}$ and 99$^{\text{th}}$ percentile WSS in the ascending aorta, see table 6. The linear regression plot is for the 99$^{\text{th}}$ percentile WSS is shown in figure 28.

CJ-FJA and WSS Linear Regression	Significance level (p)	Linear regression slope coefficient	Standard error	R^2
90$^{\text{th}}$ percentile WSS	0.61	0.032	0.062	0.015
92$^{\text{nd}}$	0.94	-0.0047	0.066	0.00028
94$^{\text{th}}$	0.44	-0.058	0.073	0.033
96$^{\text{th}}$	0.11	-0.14	0.082	0.13
98$^{\text{th}}$	0.024	-0.24	0.096	0.25
99$^{\text{th}}$	0.011	-0.30	0.11	0.31

Table 6: Linear regression results for the CJ-FJA with various percentiles of WSS in the ascending aorta

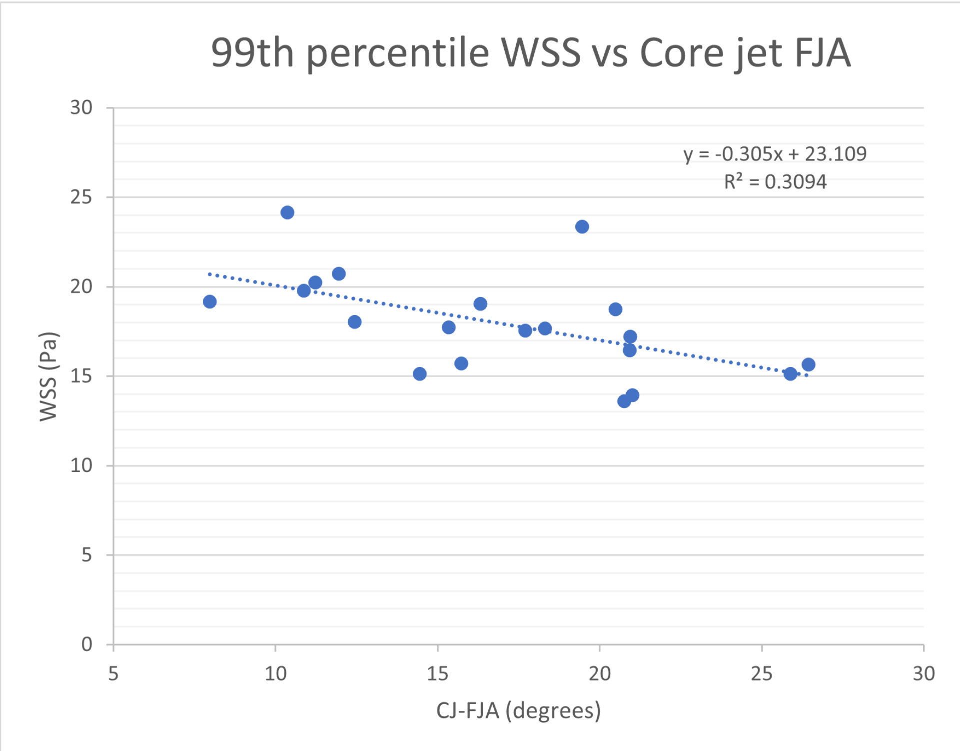

Figure 28: Graph showing 99th percentile WSS across ascending aorta plotted against the CJ-FJA of each inflow profile (p=0.011)

4.5.2 FJA

The FJA across the entire inflow profile has shown no significant results from the linear regression analysis.

FJA and WSS Linear Regression	Significance level (p)	Linear regression slope coefficient	Standard error	R^2
90^{th} percentile WSS	0.067	-0.065	0.033	0.17
92^{nd}	0.10	-0.061	0.036	0.14
94^{th}	0.25	-0.050	0.042	0.072
96^{th}	0.55	-0.031	0.051	0.020
98^{th}	0.74	-0.022	0.064	0.0062
99^{th}	0.76	-0.023	0.075	0.0051

Table 7: Linear regression results for the FJA with various percentiles of WSS in the ascending aorta

4.5.3 Flow rate

The flow rate has been shown to have a significant positive correlation with the 90^{th} percentile, see table 8. The flow rate does not have any statistically significant correlation for peak or high percentile (95+) WSS. See figure 29 for the 90^{th} percentile WSS plotted against the flow rate.

Flow rate and WSS Linear Regression	Significance level (p)	Linear regression slope coefficient	Standard error	R^2
90^{th} percentile WSS	0.0023	27.7	7.82	0.41
92^{nd}	0.011	25.2	8.86	0.31
94^{th}	0.082	20.4	11.1	0.16
96^{th}	0.38	12.7	14.1	0.044
98^{th}	0.70	6.95	17.9	0.0083
99^{th}	0.80	5.30	21.0	0.0035

Table 8: Linear regression results for the flow rate with various percentiles of WSS in the ascending aorta

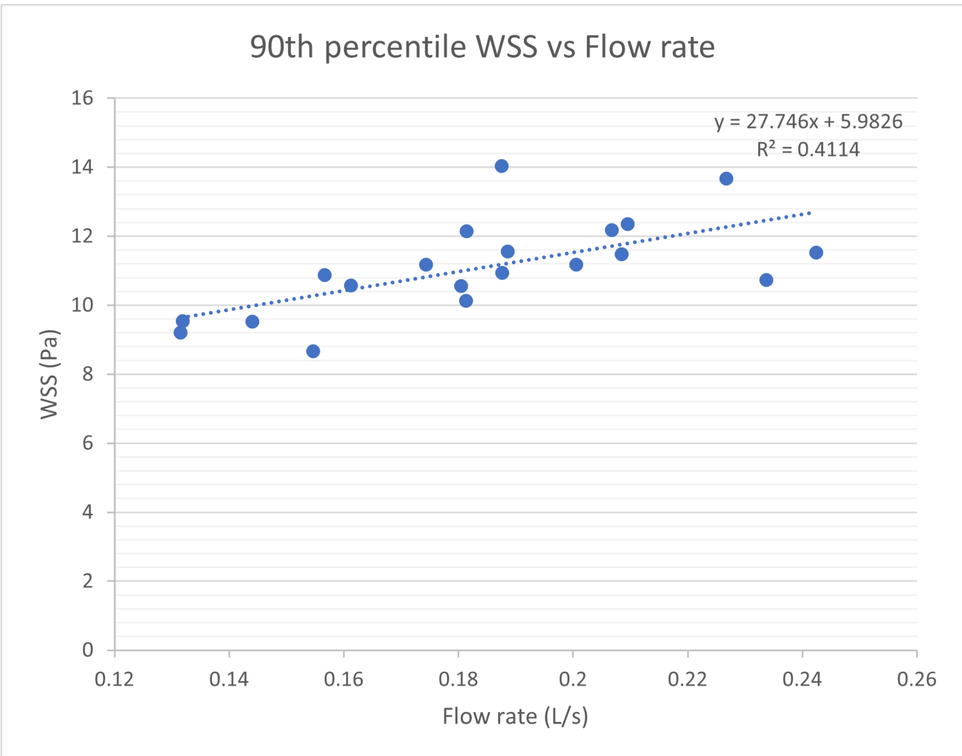

Figure 29: Graph showing 90th percentile WSS across ascending aorta plotted against the flow rate of each inflow profile (p=0.0023)

4.5.4 Other variables

None of the other inflow variables, secondary inflow angle and eccentricity, showed any significant correlation with 80+ percentile WSS, see Appendix E. Using multi-variable linear regression for all inflow variables that were tested, showed that only the CJ-FJA has a significant correlation with 99th percentile WSS, see tables 9 and 10. In table 10 the non-significant secondary angle variable from table 9 is removed, and from table 10 only the CJ-FJA is signficant ($p < 0.05$).

Multivariable linear regression with 99th WSS	Significance level (p)	Linear regression slope coefficient	Standard error	R^2 for all variables
CJ-FJA	0.0017	-0.38	0.10	0.56
Secondary angle	0.12	0.046	0.028	
Flow rate	0.045	37200	17000	
Eccentricity	0.029	3050	1260	

Table 9: Multivariable linear regression results with 99th WSS in the ascending aorta

Multivariable linear regression with 99th WSS	Significance level (p)	Linear regression slope coefficient	Standard error	R^2 for all variables
CJ-FJA	0.0030	-0.37	0.11	0.48
Flow rate	0.072	34300	17800	
Eccentricity	0.11	1740	1040	

Table 10: Multivariable linear regression results with 99th WSS in the ascending aorta, excluding the secondary angle

5 Discussion

Previous studies about aortic flow mostly use 4D flow MRI [71, 72, 73, 74, 75, 76, 77, 78], with some of them showing that a higher FJA leads to higher WSS [8, 81]. 4D flow MRI has been shown to be insufficient for accurately capturing WSS [79], with CFD allowing a more accurate way of extracting WSS [80]. This study uses CFD to focus on the effect of the FJA on WSS. The workflow developed in this study allows automatic generation of meshes and Fluent cases from datasets of aortic STL files and aortic inflow velocity profile VTP files. 20 simulations were prepared and run using the same aortic geometry and mesh using 20 different realistic inflow velocity profiles filtered from a large dataset such that the FJA is the major difference between the profiles.

5.1 Core jet FJA

The FJA is the angle at which blood flows into the aorta and has been shown to have an impact on the WSS [8, 81]. In this study the core jet FJA (CJ-FJA) is looked at as well, as it is thought to be of more relevance to peak WSS than FJA, which has also been shown by the significant CJ-FJA and peak WSS linear regression results from section 4.5.1 and insignificant FJA and peak WSS linear regression results from section 4.5.2. The CJ-FJA is defined as the FJA using only 10% of the inflow area with the highest velocity magnitude. This area with high velocity magnitude is relevant to peak WSS, as flow from that part hits the aortic wall at a higher velocity than flow from other parts of the inflow profile.

The impingement angle, the angle at which (jet) flow hits a wall, is also relevant to peak WSS, as Fillingham et al. [9] has showed that lower jet impingement angles leads to lower normalized maximum WSS values. Fillingham et al. used CFD to determine non-dimensional (normalized) WSS as a function of nozzle parameters and the impingement angle. The impingement angle was varied between 30 and 90 degrees, see figure 5 for a visual description of the impingement angle.

Determining the impingement angles for this study is difficult, so there are no calculated impingement angles. The difficulty lies in what part of the flow to choose, as it is a mix of high and low velocity magnitude flow. Other works [9, 8] that determined the impingement angle only use a consistent high velocity jet at the inlet with no low velocity flow at other parts of the inlet. Another part of the difficulty can be seen in figure 24, where it is not clear for the bottom visualization where to consider the point of impact, as the jet has a slight bend before it hits the wall. For the top visualization of figure 24 the angle can easily be determined as it follows a straight line, but for the bottom visualization the jet flow is more spread out, continues flowing near the wall and does not follow a straight line. There are also no clear guides as to how you would determine the impingement angle for CFD with complicated flow and geometry.

Despite the difficulty, a visual inspection of figure 24 seems to show that the flow from the inflow profile with lower CJ-FJA has a higher impingement angle as compared to the higher CJ-FJA inflow profile.

Hojin et al. [8] showed that for higher FJA, at multiple secondary inflow angles, there was higher 95^{th} percentile and max WSS in the thoracic aorta, caused by the jet dissipating before it hits an aortic wall at low FJA jet flow. Hojin et al. used a 3D-printed patient specific aortic vascular phantom together with a centrifugal pump to recreate systolic flow at various values for the FJA. The experiments were measured using 4D flow MRI. The flow seems to mainly consist of a consistent high velocity jet at the inlet at various angles, with other parts of the inlet not providing any flow. There are 9 total cases at FJA values of 0, 15 and 30 at 4 different secondary angles, with all cases being tested twelve times. A higher FJA showed a significant ($p < 0.01$) positive relationship with top 5% percentile WSS, using SPSS Statistics (statistical analysis software) with data tested for a normal distribution with the Shapiro-Wilk test. The flow rate used in the test is equivalent to a systolic flow rate of 0.42 L/s. As Hojin et al's work uses mainly a high velocity jet with no other flow from the inlet, the FJA is equivalent to the CJ-FJA from this study.

Comparing Hojin et al.'s [8] work to this study, the main difference are: An opposite relation found between the CJ-FJA and peak WSS, a higher flow rate used by Hojin et al. with this study having a range of flow rate of between 0.13 and 0.24 L/s, earlier dissipation of jet flow in Hojin et al's work, the use of 4D flow MRI and possibly a difference in aortic geometry used. The earlier dissipation of the jet flow could be the reason for the difference in the CJ-FJA and peak WSS relation, as the dissipation is not as significant in this study.

The impingement angle is also calculated in Hojin et al's [8] work and it seems to show an association with the FJA such that a higher FJA would lead to a lower impingement angle, but there is no mention of statistical significance. Hojin et al. do note that for right- and anterior-direction flow the impingement angle was reduced when the FJA was increased.

Bissell et al. [81] showed that increasing FJA was associated with higher rotational flow values (intergral of vorticity across aortic cross-section, also refered to as ’circulation’), which causes the jet to hit an aortic wall at a higher impingement angle, which results in more of the jet rotating along the aortic walls and leading to an increase in WSS. Bissell et al. used 4D flow MRI to acquire 4D velocity fields of 142 subjects with BAV disease. From these velocity fields WSS is directly computed. The systolic flow angle from Bissel et al. is equivalent to the FJA from this study, and not the CJ-FJA.

The results from Bissel et al. [81] are not in line with results from this study (assuming that CJ-FJA from this study can reasonably be compared to the systolic flow angle from Bissel et al.), although it is unclear if the increase in WSS from the work of Bissell et al. also includes peak WSS in the ascending aorta. The difference may come from this study being more controlled around the (CJ-)FJA while Bissel et al.'s work is more general and uses patient-specific aortic geometry and velocity fields.

The strengths of this study compared to others [8, 81] are: the focus on purely the (CJ-)FJA, the use of CFD to more accurately capture WSS as compared to 4D flow MRI and the use of realistic inflow velocity profiles. This study has shown a significant negative relationship between the CJ-FJA and peak WSS and a possible relationship between the (CJ-)FJA, the impingement angle and WSS. Other work has shown a definite relationship between the impingement angle and peak WSS [9] and other work has shown a positive relationship between the FJA and WSS [8, 81]. From this it is fair to conclude that a higher (CJ-)FJA does not necessarily induce lower peak WSS, but can lead to different jet flows that can hit an aortic wall at various angles leading to various WSS values depending on the impingement angle, which also depends on the aortic geometry, and other factors like the peak positive velocity (PPV). The travel length until a jet dissipates is also relevant, but is also highly aortic geometry and inflow dependent. For future studies, it is recommended to also include impingement angle when studying relationship of WSS in the ascending aorta with inflow or geometric parameters. For the specific aortic geometry used in this work, a higher CJ-FJA seems to lead to lower peak WSS (99^{th} percentile).

5.2 Secondary angle

The secondary angle was not considered when choosing the inflow velocity profiles, but was shown to not have significant results relating to WSS. It is unlikely that the secondary angle would have a significant effect on invalidating the linear regression results of the (CJ-)FJA and WSS, as even with the highest secondary angle (see figures 18, 19, 20 and 21), the jet flow hits the aortic wall within the ascending aorta at approximately the same location as the other inflow profiles shown in figures 14, 15, 16 and 17. All the secondary angles in the used inflow velocity profiles occur in a total range of 90 degrees, so there is no significant change in jet orientation between the profiles used.

5.3 Flow rate

The significant correlation between flow rate and 90^{th} percentile WSS is logical, as higher flow rate mean general higher velocity in the aorta and WSS is directly associated with velocity, see equation 1. It also expected that no significant correlation could be found for higher percentile WSS, as the inflow velocity profiles were filtered from the dataset such that the peak velocity would be roughly the same for all inflow profiles.

5.4 Computational workflow

The workflow for automatically generating multiple meshes and Fluent cases based on different aortic geometry STL files and inflow velocity profiles VTP files is beneficial in saving the time needed for manually creating them. A hundred different meshes and Fluent cases based on different aortic geometric can be made in 11 hours by activating a script like the one in Appendix B.1, assuming a polyhedral mesh of 5 million cells. This script can easily be altered by using Ansys Workbench to record all actions taken for a single manual mesh and case generation, which is logged in a script file, and altering the logged script using Python language.

6 Research limitations

In this study, there were some simplifications made in order to be able to assess the various inflow profiles in a reasonable time frame. The major simplification is the use of only peak systolic flow without consideration for the aortic cycle. It is hard to tell how unrealistic the flow in time is, but averaging the WSS across time for each simulation should hopefully make the averaged results be close to how the WSS (within the ascending aorta) would look like for the moment the systolic jet flow impinges on the aortic wall.

Other limitations include: timestep such that Courant number is above a 1, the use of rigid walls, the use of laminar flow while the inlet flow has Reynolds number of 3000 indicating hard to model transition flow. The impact of the Courant number on the regression modelling should be minimal, since I am only looking at data averaged across time in transient simulations for inflow profiles that do not change in time.

The usage of rigid walls has a low impact on TAWSS and a significant impact on instantaneous WSS [24]. This study uses average WSS across time for transient simulations of systolic peak flow, which could be seen as using time averaging to estimate the instantaneous WSS systolic peak flow would have in the cardiac cycle. How the use of rigid wall affects this specific situation is unclear.

The usage of laminar flow has been shown to significantly underestimate WSS compared to LES models [64], but that it can also estimate TAWSS close to LES values if the laminar model is well resolved [35]. Compared to Manchester et al. [35] this work has a similar mesh quality but lower timestep quality, making it unclear if this laminar flow study would be considered well resolved enough to estimate TAWSS like LES models.

The simplification of no branches might be fine for this WSS-shape correlation research, as most (70% [88]) of the flow within the ascending aorta goes towards the descending aorta area. Also, the branches are not within the ascending aorta, but near the aortic arch, which lessens the impact they have on the flow and WSS within the ascending aorta. Studies that investigated the effect of removing these branches for simplification showed that the WSS across the entire aorta was significantly altered [89] and the WSS near false lumens (mostly in the descending aorta) was significantly altered [90].

7 Recommendations for future work

A list of recommendations for future work is shown below:

- Simulating various inflow profiles together with various aortic geometries. This could show if the effect of the FJA on WSS found in this study, and possibly other inflow variables, holds up for varying aortic geometries.
- The same study as this thesis could be done, but with a focus on aortas of healthy young people to see if aortas at risk can be found, as existing work mainly focuses on old people with an ascending thoracic aortic aneurysm. Results from such a study could be used to find young people at risk of long-term damage to aorta walls and thus also people who may suffer from an aneurysm (far) in the future.
- Inclusion of impingement angle of aortic inflow on the aortic wall in future work, as this variable has significant effect on peak WSS if there is a jet flow. This will require the development of a tool to reliably calculate the impingement angle a jet has on the aortic wall.
- Inclusion of the full aortic cycle in the aortic inflow to see if the association between FJA and WSS holds up.
- Research if disrupting aortic jet flow could reduce (peak) WSS within the ascending aorta, which could be useful if applied to aortic reconstruction. The idea is that disrupting the jet would spread around the force of the jet unto a larger aortic wall area, which should lower peak WSS, which could hopefully also lower aortic wall degradation.
- Repeat the work done in this thesis, but with a focus on other aortic inflow variables, like FDI. This is within reach with the modelling workflow established in this thesis.
- Investigate the effect of different ascending aorta phenotypes. The phenotype shows the general shape of the ascending aorta, so it is expected that this would have a big influence on how the aortic jet flow hits a wall, which could give different results when comparing FJA and WSS in the ascending aorta.
- Perform a study to see the effect aortic geometry simplifications have on WSS results and WSS correlations with shape and inflow parameters, with a focus on removal and inclusion of branches. If such a study shows no significant differences within the ascending aorta, future work focused on the ascending aorta could be simplified with the removal of branches.

8 Conclusion

In this study, a workflow process to work with a large amount of aortic geometries and inflow profiles has been established for working with aortic flow with a single inlet and outlet. With this process, transient simulations of 20 different inflow profiles at systolic peak flow were done with main intent of finding the effect the flow jet angle has on ascending aortic wall shear stress. From the results, the main research question can be answered as follows: The core flow jet angle is significantly negatively correlated with peak wall shear stress within the ascending aorta and flow rate is significantly positively correlated with overall wall shear stress in the ascending aorta for the specific aortic geometry used. As other works show positive correlations of the flow jet angle and the wall shear stress, it is recommended to investigate other flow variables, like the aortic jet impingement angle, as that has been shown to have a significant effect on peak wall shear stress.

References

[1] *Ascending Aortic Aneurysm.* URL: https://my.clevelandclinic.org/health/diseases/21949-ascending-aortic-aneurysm. (accessed: 31.08.2022).

[2] Howard D.P.J. et al. "Population-Based Study of Incidence and Outcome of Acute Aortic Dissection and Premorbid Risk Factor Control 10-Year Results From the Oxford Vascular Study". In: *Circulation* 127.20 (2013), pp. 2031–2037.

[3] Salmasi M.Y. et al. "High Wall Shear Stress can Predict Wall Degradation in Ascending Aortic Aneurysms: An Integrated Biomechanics Study". In: *Front Bioeng Biotechnol.* (2021).

[4] Youssefi P. et al. "Functional assessment of thoracic aortic aneurysms - the future of risk prediction?" In: *Br Med Bull.* 121.1 (2017), pp. 61–71.

[5] Barker A.J. et al. "Bicuspid aortic valve is associated with altered wall shear stress in the ascending aorta". In: *Circ Cardiovasc Imaging.* 5.4 (2012), pp. 457–466.

[6] Callaghan F.M. et al. "Normal patterns of thoracic aortic wall shear stress measured using four-dimensional flow MRI in a large population." In: *American Journal of Physiology-Heart and Circulatory Physiology* 315.5 (2018), pp. 1174–1181.

[7] Cosentino F. et al. "Statistical Shape Analysis of Ascending Thoracic Aortic Aneurysm: Correlation between Shape and Biomechanical Descriptors". In: *Journal of Personalized Medicine* 10.2 (2020), pp. 1438–1449.

[8] Hojin H. et al. "The influence of the aortic valve angle on the hemodynamic features of the thoracic aorta". In: *Scientific reports* 6.1 (2016), pp. 1–14.

[9] Fillingham P. et al. "Model for Wall Shear Stress from Obliquely Impinging Planar Underexpanded Jets". In: *Applied Sciences* 12.14 (2022), p. 7311.

[10] Wikipedia contributors. *Cardiac output — Wikipedia, The Free Encyclopedia.* [Online; accessed 23-November-2022]. 2022. URL: https://en.wikipedia.org/w/index.php?title=Cardiac_output&oldid=1106874812.

[11] Wendell D.C. et al. "Including aortic valve morphology in computational fluid dynamics simulations: initial findings and application to aortic coarctation". In: *Medical engineering & physics* 35.6 (2013), pp. 723–735.

[12] Youssefi P. et al. "Impact of patient-specific inflow velocity profile on hemodynamics of the thoracic aorta". In: *Journal of biomechanical engineering* 140.1 (2018).

[13] Wikipedia contributors. *Aorta — Wikipedia, The Free Encyclopedia.* [Online; accessed 23-November-2022]. 2022. URL: https://en.wikipedia.org/w/index.php?title=Aorta&oldid=1122593855.

[14] Wikipedia contributors. *Systole — Wikipedia, The Free Encyclopedia.* [Online; accessed 23-November-2022]. 2022. URL: https://en.wikipedia.org/w/index.php?title=Systole&oldid=1104666352.

[15] Romero P. et al. "Clinically-Driven Virtual Patient Cohorts Generation: An Application to Aorta". In: *Frontiers in Physiology* (2021).

[16] Craiem D. et al. "Aging impact on thoracic aorta 3D morphometry in intermediate-risk subjects: looking beyond coronary arteries with non-contrast cardiac CT". In: *Annals of biomedical engineering* 40.5 (2012), pp. 1028–1038.

[17] Schaefer B.M. et al. "The bicuspid aortic valve: an integrated phenotypic classification of leaflet morphology and aortic root shape". In: *Heart* 94.12 (2008), pp. 1634–1638.

[18] Della Corte A. et al. "The ascending aorta with bicuspid aortic valve: a phenotypic classification with potential prognostic significance". In: *European Journal of Cardio-Thoracic Surgery* 46.2 (2014), pp. 240–247.

[19] Thamsen B. et al. "Synthetic database of aortic morphometry and hemodynamics: overcoming medical imaging data availability". In: *IEEE Transactions on Medical Imaging* 40.5 (2021), pp. 1438–1449.

[20] Lantz J. et al. "Quantifying turbulent wall shear stress in a subject specific human aorta using large eddy simulation". In: *Medical engineering & physics* 34.8 (2012), pp. 1139–1148.

[21] McClarty D. et al. "Ascending aortic aneurysm haemodynamics are associated with aortic wall biomechanical properties". In: *European Journal of Cardio-Thoracic Surgery* 61.2 (Oct. 2021), pp. 367–375. ISSN: 1010-7940. DOI: 10.1093/ejcts/ezab471. eprint: https://academic.oup.com/ejcts/article-pdf/61/2/367/42268568/ezab471.pdf. URL: https://doi.org/10.1093/ejcts/ezab471.

[22] University College London. *Fluid Mechanics II Viscosity and shear stresses.* [Online; accessed 07-June-2023]. 2011. URL: https://www.homepages.ucl.ac.uk/~uceseug/Fluids2/Notes_Viscosity.pdf.

[23] S., Seal. *Deriving the Newton's law of Viscosity —English— —Part 1—.* [Online; accessed 07-June-2023]. 2020. URL: https://www.youtube.com/watch?v=69L0CeCzNf4.

[24] Lantz J. et al. "Wall shear stress in a subject specific human aorta—influence of fluid-structure interaction". In: *International Journal of Applied Mechanics* 3.04 (2011), pp. 759–778.

[25] Mahalingam A. et al. "Numerical analysis of the effect of turbulence transition on the hemodynamic parameters in human coronary arteries". In: *Cardiovascular diagnosis and therapy* 6.3 (2016), p. 208.

[26] Vinoth R. et al. "Steady and transient flow CFD simulations in an aorta model of normal and aortic aneurysm subjects". In: (2017), pp. 29–43.

[27] Pasta S. et al. "Shear stress and aortic strain associations with biomarkers of ascending thoracic aortic aneurysm". In: *The Annals of thoracic surgery* 110.5 (2020), pp. 1595–1604.

[28] Pasta S. et al. "In silico shear and intramural stresses are linked to aortic valve morphology in dilated ascending aorta". In: *European Journal of Vascular and Endovascular Surgery* 54.2 (2017), pp. 254–263.

[29] Lee D. et al. "Numerical simulation of steady flow fields in a model of abdominal aorta with its peripheral branches". In: *Journal of biomechanics* 35.8 (2002), pp. 1115–1122.

[30] Wikipedia contributors. *Womersley number — Wikipedia, The Free Encyclopedia.* [Online; accessed 23-November-2022]. 2022. URL: https://en.wikipedia.org/w/index.php?title=Womersley_number&oldid=1085515656.

[31] Vincent P.E. et al. "Blood flow in the rabbit aortic arch and descending thoracic aorta". In: *Journal of The Royal Society Interface* 8.65 (2011), pp. 1708–1719.

[32] Paruchuri V. et al. "Aortic size distribution in the general population: explaining the size paradox in aortic dissection". In: *Cardiology* 131.4 (2015), pp. 265–272.

[33] Avram R. et al. "Real-world heart rate norms in the Health eHeart study". In: *NPJ digital medicine* 2.1 (2019), p. 58.

[34] Gijsen F. et al. "Expert recommendations on the assessment of wall shear stress in human coronary arteries: existing methodologies, technical considerations, and clinical applications". In: *European heart journal* 40.41 (2019), pp. 3421–3433.

[35] Manchester E.L. et al. "Evaluation of Computational Methodologies for Accurate Prediction of Wall Shear Stress and Turbulence Parameters in a Patient-Specific Aorta". In: *Frontiers in bioengineering and biotechnology* 10 (2022).

[36] Renner J. et al. "Is a flat inlet profile sufficient for WSS estimation in the aortic arch". In: *WSEAS Transactions on Fluid Mechanics* 4.4 (2009), pp. 148–160.

[37] Mohamied Y et al. "Understanding the fluid mechanics behind transverse wall shear stress". In: *Journal of Biomechanics* 50 (2017), pp. 102–109.

[38] Bessonov N. et al. "Methods of blood flow modelling". In: *Mathematical modelling of natural phenomena* 11.1 (2016), pp. 1–25.

[39] Pedley T.J. *The Fluid Mechanics of Large Blood Vessels.* Cambridge Monographs on Mechanics. Cambridge University Press, 1980. DOI: 10.1017/CBO9780511896996.

[40] Cabalerro A.D. et al. "A review on computational fluid dynamics modelling in human thoracic aorta". In: *Cardiovascular Engineering and Technology* 4.2 (2013), pp. 103–130.

[41] Khan M. et al. "On multiple solutions of non-Newtonian Carreau fluid flow over an inclined shrinking sheet". In: *Results in physics* 8 (2018), pp. 926–932.

[42] Wikipedia contributors. *Carreau fluid — Wikipedia, The Free Encyclopedia.* [Online; accessed 23-November-2022]. 2022. URL: https://en.wikipedia.org/w/index.php?title=Carreau_fluid&oldid=1110572065.

[43] Soulis J.V. et al. "Relative residence time and oscillatory shear index of non-Newtonian flow models in aorta". In: *2011 10th international workshop on biomedical engineering.* IEEE. 2011, pp. 1–4.

[44] Petuchova A. et al. "Comparison Of Newtonian and Non-Newtonian Blood Flow in an Ascending Aortic Aneurysm". In: *Computing in Cardiology* (2022).

[45] Perktold K. et al. "Pulsatile non-Newtonian blood flow simulation through a bifurcation with an aneurysm". In: *Biorheology* 26.6 (1989), pp. 1011–1030.

[46] Casa L.D.C. et al. “Role of high shear rate in thrombosis”. In: *Journal of vascular surgery* 61.4 (2015), pp. 1068–1080.

[47] Ballyk P.D. et al. “Simulation of non-Newtonian blood flow in an end-to-side anastomosis”. In: *Biorheology* 31.5 (1994), pp. 565–586.

[48] Perktold K. et al. “Pulsatile non-Newtonian flow characteristics in a three-dimensional human carotid bifurcation model”. In: (1991).

[49] Sacks A.H. et al. “The compressibility of blood”. In: *Biorheology* 5.4 (1968), pp. 271–274.

[50] Wikipedia contributors. *Properties of water — Wikipedia, The Free Encyclopedia.* [Online; accessed 26-October-2022]. 2022. URL: https://en.wikipedia.org/w/index.php?title=Properties_of_water&oldid=1116435711.

[51] Miyazaki S. et al. “Validation of numerical simulation methods in aortic arch using 4D Flow MRI”. In: *Heart and Vessels* 32.8 (2017), pp. 1032–1044.

[52] ANSYS, Inc. *Continuity and Momentum Equations.* [Online; accessed 7-June-2023]. 2009. URL: https://www.afs.enea.it/project/neptunius/docs/fluent/html/th/node11.htm.

[53] Wikipedia contributors. *Continuity equation — Wikipedia, The Free Encyclopedia.* [Online; accessed 7-June-2023]. 2023. URL: https://en.wikipedia.org/wiki/Continuity_equation.

[54] Wikipedia contributors. *Navier–Stokes equations — Wikipedia, The Free Encyclopedia.* [Online; accessed 7-June-2023]. 2023. URL: https://en.wikipedia.org/wiki/Navier-Stokes_equations.

[55] Pirola S. et al. “4-D flow MRI-based computational analysis of blood flow in patient-specific aortic dissection”. In: *IEEE Transactions on Biomedical Engineering* 66.12 (2019), pp. 3411–3419.

[56] Wimshurst A. *[CFD] How Fine should my CFD mesh be?* Youtube. 2019. URL: https://www.youtube.com/watch?v=60fDz2cVdy8.

[57] Wimshurst A. *[CFD] What are Wall Functions and How do they work?* Youtube. 2018. URL: https://www.youtube.com/watch?v=fJDYtEGMgzs.

[58] *Courant number in CFD.* [Online; accessed 21-may-2023]. Apr. 2022. URL: https://www.idealsimulations.com/resources/courant-number-cfd/.

[59] Stein P.D. et al. “Turbulent blood flow in the ascending aorta of humans with normal and diseased aortic valves.” In: *Circulation research* 39.1 (1976), pp. 58–65.

[60] Cadence CFD. *Examining Reynolds Number For Turbulent Flow.* [Online; accessed 02-June-2023]. 2022. URL: https://resources.system-analysis.cadence.com/blog/msa2022-examining-reynolds-number-for-turbulent-flow.

[61] Engineering ToolBox. *Laminar, Transitional and Turbulent Flow.* [Online; accessed 02-June-2023]. 2004. URL: https://www.engineeringtoolbox.com/laminar-transitional-turbulent-flow-d_577.html.

[62] Febina J. et al. “Wall shear stress estimation of thoracic aortic aneurysm using computational fluid dynamics”. In: *Computational and mathematical methods in medicine* 2018 (2018).

[63] Liepsch D., ST Moravec, and R Baumgart. “Some flow visualization and laser-Doppler-velocity measurements in a true-to-scale elastic model of a human aortic arch—a new model technique”. In: *Biorheology* 29.5-6 (1992), pp. 563–580.

[64] Manchester E.L. et al. “Analysis of turbulence effects in a patient-specific aorta with aortic valve stenosis”. In: *Cardiovascular engineering and technology* 12.4 (2021), pp. 438–453.

[65] Santos S. et al. “Analysis of turbulence models for flow simulation in the aorta”. In: *Proceedings of the XXVI Congreso de Ecuaciones Diferenciales y Aplicaciones. XVI Congreso de Matemática Aplicada.* Servicio de Publicaciones de la Universidad de Oviedo. 2021.

[66] Armour C.H. et al. “The influence of inlet velocity profile on predicted flow in type B aortic dissection”. In: *Biomechanics and modeling in mechanobiology* 20.2 (2021), pp. 481–490.

[67] Markl M. et al. “4D flow MRI”. In: *Journal of Magnetic Resonance Imaging* 36.5 (2012), pp. 1015–1036.

[68] Pirola S. et al. “Computational study of aortic hemodynamics for patients with an abnormal aortic valve: The importance of secondary flow at the ascending aorta inlet”. In: *APL bioengineering* 2.2 (2018), p. 026101.

[69] Saitta S. et al. “Data-driven generation of 4D velocity profiles in the aneurysmal ascending aorta”. In: *arXiv preprint arXiv:2211.00551* (2022).

[70] Kiema M. et al. “Wall Shear Stress Predicts Media Degeneration and Biomechanical Changes in Thoracic Aorta”. In: *Front Physiol.* (2022).

[71] van Ooij P. et al. “Characterization of abnormal wall shear stress using 4D flow MRI in human bicuspid aortopathy”. In: *Annals of biomedical engineering* 43 (2015), pp. 1385–1397.

[72] Catapano F. et al. “4D flow imaging of the thoracic aorta: is there an added clinical value?” In: *Cardiovascular Diagnosis and Therapy* 10.4 (2020), p. 1068.

[73] Rodrıguez-Palomares J.F. et al. “Aortic flow patterns and wall shear stress maps by 4D-flow cardiovascular magnetic resonance in the assessment of aortic dilatation in bicuspid aortic valve disease”. In: *Journal of Cardiovascular Magnetic Resonance* 20.1 (2018), pp. 1–15.

[74] Lee S. et al. “Evaluation of flow pattern in the ascending aorta in patients with repaired tetralogy of Fallot using four-dimensional flow magnetic resonance imaging”. In: *Korean journal of radiology* 20.9 (2019), pp. 1334–1341.

[75] Rose M.J. et al. “4-D flow MRI aortic 3-D hemodynamics and wall shear stress remain stable over short-term follow-up in pediatric and young adult patients with bicuspid aortic valve”. In: *Pediatric radiology* 49 (2019), pp. 57–67.

[76] Soulat G. et al. “4D flow with MRI”. In: *Annual review of biomedical engineering* 22 (2020), pp. 103–126.

[77] Doyle C.M. et al. “Four-dimensional flow magnetic resonance imaging in the assessment of blood flow in the heart and great vessels: A systematic review”. In: *Journal of Magnetic Resonance Imaging* 55.5 (2022), pp. 1301–1321.

[78] Dyverfeldt P. et al. “4D flow cardiovascular magnetic resonance consensus statement”. In: *Journal of Cardiovascular Magnetic Resonance* 17.1 (2015), pp. 1–19.

[79] Piatti F. et al. “Towards the improved quantification of in vivo abnormal wall shear stresses in BAV-affected patients from 4D-flow imaging: Benchmarking and application to real data”. In: *Journal of biomechanics* 50 (2017), pp. 93–101.

[80] Salmasi M. et al. “Geometry and flow in ascending aortic aneurysms are influenced by left ventricular outflow tract orientation: Detecting increased wall shear stress on the outer curve of proximal aortic aneurysms”. In: *The Journal of Thoracic and Cardiovascular Surgery* (2021).

[81] Bissell M.M. et al. “Aortic dilation in bicuspid aortic valve disease: flow pattern is a major contributor and differs with valve fusion type”. In: *Circulation: Cardiovascular Imaging* 6.4 (2013), pp. 499–507.

[82] O’Donovan T.S. et al. “Fluctuating fluid flow and heat transfer of an obliquely impinging air jet”. In: *International Journal of heat and mass transfer* 51.25-26 (2008), pp. 6169–6179.

[83] Sosnowski M. et al. “Polyhedral meshing in numerical analysis of conjugate heat transfer”. In: *European Physical Journal Web of Conferences*. Vol. 180. European Physical Journal Web of Conferences. Nov. 2018, 02096, p. 02096. DOI: `10.1051/epjconf/201818002096`.

[84] LuckyTran. *Simple vs Piso*. [Online; accessed 19-June-2023]. 2018. URL: `https://www.cfd-online.com/Forums/fluent/211720-simple-vs-piso.html`.

[85] Chudzicki C. *Math3D*. `https://github.com/ChristopherChudzicki`. [Online; accessed 21-May-2023]. 2013.

[86] Pirola S. et al. “On the choice of outlet boundary conditions for patient-specific analysis of aortic flow using computational fluid dynamics”. In: *Journal of biomechanics* 60 (2017), pp. 15–21.

[87] Mori D. et al. “Computational fluid dynamics modeling and analysis of the effect of 3-D distortion of the human aortic arch”. In: *Computer Methods in Biomechanics & Biomedical Engineering* 5.3 (2002), pp. 249–260.

[88] Raffa G.M. et al. “Ascending Aorta Resection and End-to-End Anastomosis: Redistribution of Wall Shear Stress Induced by a Bioprosthetic Heart Valve”. In: *Prosthesis* 2.4 (2020), pp. 297–303.

[89] Yevtushenko P. et al. “Numerical investigation of the impact of branching vessel boundary conditions on aortic hemodynamics”. In: *Current Directions in Biomedical Engineering* 3.2 (2017), pp. 321–324.

[90] Jiang Y. et al. “Influence of aortic branch arteries on the hemodynamics of patient-specific type B aortic dissection following TEVAR”. In: *Medicine in Novel Technology and Devices* 4 (2019), p. 100028.

A OpenFOAM related code

A.1 Shell script file for the looping of generating meshes with OpenFOAM to be inputted into Fluent

```
#!/bin/sh

rm fluentInterface/*
rm MeshCheck.txt
touch MeshCheck.txt
for i in `seq 10 15`
do
  rm surfaceMeshes/*
  rm VTK/*
  rm inlet.stl
  rm outlet.stl
  rm wall.stl
  rm AortaNewTest.stl

  cp STLaortaFiles/case_00${i}/meshes/* .

  sed -i 's/ascii/inlet/g' inlet.stl
  sed -i 's/ascii/outlet/g' outlet.stl
  sed -i 's/ascii/wall/g' wall.stl
  cat inlet.stl newline.stl outlet.stl newline.stl wall.stl > AortaNewTest.stl
  surfaceToFMS AortaNewTest.stl
  mv AortaNewTest.fms surfaceMeshes/
  cartesianMesh
  transformPoints -scale "(0.001 0.001 0.001)"
  checkMesh | tail -n 4 >> MeshCheck.txt
  echo "$i" >> MeshCheck.txt
  foamMeshToFluent
  mv fluentInterface/CFMesh_FluentSetupMeshGenerator.msh fluentInterface/CFMeshTest${i}.msh

  foamToVTK
  mv VTK/CFMesh_FluentSetupMeshGenerator_0/boundary/inlet.vtp VTK_Output/inlet_00${i}.vtp
done
```

A.2 MeshDict file for generating meshes with cfMesh in OpenFoam

```
/*--------------------------------*- C++ -*----------------------------------*\
|    _ _ _ _    |                                                             |
| //         \\ | Creative Fields CF-MESH+                                    |
| | CF-MESH+  | |                                                             |
| \\ _ _ _ _ // | Version: 3.2.1                                              |
|               | Web: www.c-fields.com e-mail: support@c-fields.com          |
\*---------------------------------------------------------------------------*/
FoamFile
{
version 2;
format  ascii;
class dictionary;
location  "system";
object  meshDict;
}

// * * * * * * * * * * * * * * * * * * * * * * * * * * * * * * * * * * * * //
checkForGluedMesh 1;
keepCellsIntersectingBoundary 1;
maxCellSize 2.3; // 2.3 and local refinement level =4 may also give good results
//boundaryCellSize 0.7
meshMultipleDomainsAndBaffles 0;
nCellsBetweenLevels 0;
snappingFactor  3;
//surfaceFile "surfaceMeshes/aorta_0.fms";
surfaceFile "surfaceMeshes/AortanewTest.fms";
boundaryLayers
{
    patchBoundaryLayers
    {
        wall
        {
            nLayers 0;
            thicknessRatio  1.4;
            totalLayerThickness 0.3;
      //maxFirstLayerThickness
      allowDiscontinuity 1;
        }
    }

}
domainDefinition
{
    convertAllPatchesToFaceZones  1;
    detachPointsAtAllInternalPatches  0;
    domainNames ();
    generateMeshInAllDomains  1;
}
keepCellsIntersectingPatches
{

}
localRefinement
{
    wall
    {
        additionalRefinementLevels  3;
    //refinementThickness         2;
    }
    inlet
    {
        additionalRefinementLevels  4;
    }
 //   outlet
 //   {
 //       additionalRefinementLevels  3;
 //   }

}
meshQualitySettings
{
    maxNonOrthogonality 65;
    maxSkewness 4;
    nPreSmoothingIterations 5;
```

```
}
objectRefinements
{

}

// ************************************************************************* //
```

B Fluent scripting code

B.1 Workbench recorded script for mesh and case generation

```
  # encoding: utf-8
# 2022 R2
SetScriptVersion(Version="22.2.192")
template1 = GetTemplate(TemplateName="FLTG")
system1 = template1.CreateSystem()
setup1 = system1.GetContainer(ComponentName="Setup")
fluentLauncherSettings1 = setup1.GetFluentLauncherSettings()
fluentLauncherSettings1.SetEntityProperties(Properties=Set(EnvPath={}, RunParallel=True, NumberOfProcessorsMeshing=4, NumberOfProcessors=4))
tGridData1 = GetDataEntity("/Mesh/TGridData:TGridData")
tGridData1.SetEntityProperties(Properties=Set(RunParallel=True, NumberOfProcs=4))
mesh1 = system1.GetContainer(ComponentName="Mesh")
Fluent.Edit(Container=mesh1)
setup1.SendCommand(Command='(cx-gui-do cx-activate-tab-index "NavigationPane*Frame1(TreeTab)" 0)(cx-gui-do cx-activate-tab-index "NavigationPane*Frame1(TreeTab)" 1)')
setup1.SendCommand(Command='/file/set-tui-version "22.2"(cx-gui-do cx-activate-tab-index "NavigationPane*Frame1(TreeTab)" 0)(cx-gui-do cx-activate-item "Key Behavioral Changes*PanelButtons*PushButton1(OK)")')
setup1.SendCommand(Command='(%py-exec "preferences.General.KeyBehavioralChangesMessage.setState(True)")')
setup1.SendCommand(Command="(%py-exec \"workflow.InitializeWorkflow(WorkflowType=r'Watertight Geometry')\")")
setup1.SendCommand(Command="(%py-exec \"meshing.GlobalSettings.LengthUnit.setState(r'mm')\")")
setup1.SendCommand(Command="(%py-exec \"meshing.GlobalSettings.AreaUnit.setState(r'mm^2')\")")
setup1.SendCommand(Command="(%py-exec \"meshing.GlobalSettings.VolumeUnit.setState(r'mm^3')\")")
setup1.SendCommand(Command="(%py-exec \"workflow.TaskObject['Import Geometry'].Arguments.setState({r'FileFormat': r'Mesh',r'ImportCadPreferences': {r'CISeparation': r'region',},r'MeshFileName': r'E:/OpenFOAM/CFMesh_FluentSetupMeshGenerator/fluentInterface/CFMeshTest10.msh',r'MeshUnit': r'mm',})\")")
setup1.SendCommand(Command="(%py-exec \"workflow.TaskObject['Import Geometry'].Execute()\")")
setup1.SendCommand(Command="(%py-exec \"workflow.TaskObject['Add Local Sizing'].AddChildToTask()\")")
setup1.SendCommand(Command="(%py-exec \"workflow.TaskObject['Add Local Sizing'].Execute()\")")
setup1.SendCommand(Command="(%py-exec \"workflow.TaskObject['Generate the Surface Mesh'].Execute()\")")
setup1.SendCommand(Command="(%py-exec \"workflow.TaskObject['Describe Geometry'].UpdateChildTasks(SetupTypeChanged=False)\")")
setup1.SendCommand(Command="(%py-exec \"workflow.TaskObject['Describe Geometry'].Arguments.setState({r'SetupType': r'The geometry consists of only fluid regions with no voids',})\")")
setup1.SendCommand(Command="(%py-exec \"workflow.TaskObject['Describe Geometry'].UpdateChildTasks(SetupTypeChanged=True)\")")
setup1.SendCommand(Command="(%py-exec \"workflow.TaskObject['Describe Geometry'].Execute()\")")
setup1.SendCommand(Command="(%py-exec \"workflow.TaskObject['Update Boundaries'].Execute()\")")
setup1.SendCommand(Command="(%py-exec \"workflow.TaskObject['Update Regions'].Execute()\")")
setup1.SendCommand(Command="(%py-exec \"workflow.TaskObject['Add Boundary Layers'].Arguments.setState({r'NumberOfLayers': 10,})\")")
setup1.SendCommand(Command="(%py-exec \"workflow.TaskObject['Add Boundary Layers'].AddChildToTask()\")")
setup1.SendCommand(Command="(%py-exec \"workflow.TaskObject['Add Boundary Layers'].InsertCompoundChildTask()\")")
setup1.SendCommand(Command="(%py-exec \"workflow.TaskObject['smooth-transition_1'].Arguments.setState({r'BLControlName': r'smooth-transition_1',r'NumberOfLayers': 10,})\")")
setup1.SendCommand(Command="(%py-exec \"workflow.TaskObject['Add Boundary Layers'].Arguments.setState({})\")")
setup1.SendCommand(Command="(%py-exec \"workflow.TaskObject['smooth-transition_1'].Execute()\")")
setup1.SendCommand(Command="(%py-exec \"workflow.TaskObject['Generate the Volume Mesh'].Arguments.setState({r'VolumeFillControls': {r'GrowthRate': 1.05,r'TetPolyMaxCellLength': 0.00042,},})\")")
setup1.SendCommand(Command="(%py-exec \"workflow.TaskObject['Generate the Volume Mesh'].Execute()\")")
setup1.SendCommand(Command='(cx-gui-do cx-activate-item "Ribbon*Frame1*Frame2(Task Page)*Table1*Table3(Solution)*PushButton1(Switch to Solution)")(cx-gui-do cx-activate-item "Question*OK")(cx-gui-do cx-activate-tab-index "NavigationPane*Frame1(TreeTab)" 1)')
setup1.SendCommand(Command="(newline)")
setup1.SendCommand(Command='(cx-gui-do cx-set-list-tree-selections "NavigationPane*Frame2*Table1*List_Tree2" (list "Setup|Boundary Conditions|Inlet|inlet (velocity-inlet, id=10)"))
```

```
')
setup1.SendCommand(Command='(cx-gui-do cx-set-list-tree-selections "NavigationPane*Frame2*Table1*List_Tree2" (list "Setup|Boundary Conditions|Inlet|inlet (velocity-inlet, id=10)"))(cx-gui-do cx-activate-item "NavigationPane*Frame2*Table1*List_Tree2")')
setup1.SendCommand(Command="(cx-gui-do cx-set-list-tree-selections \"NavigationPane*Frame2*Table1*List_Tree2\" (list \"Setup|Boundary Conditions|Inlet|inlet (velocity-inlet, id=10)\"))(cx-gui-do cx-activate-tab-index \"Velocity Inlet*Frame2*Frame2\" 0)(cx-gui-do cx-activate-tab-index \"Velocity Inlet*Frame2*Frame2\" 1)(cx-gui-do cx-activate-tab-index \"Velocity Inlet*Frame2*Frame2\" 0)(cx-gui-do cx-activate-tab-index \"Velocity Inlet*Frame2*Frame2\" 2)(cx-gui-do cx-activate-tab-index \"Velocity Inlet*Frame2*Frame2\" 0)(cx-gui-do cx-activate-tab-index \"Velocity Inlet*Frame2*Frame2\" 3)(cx-gui-do cx-activate-tab-index \"Velocity Inlet*Frame2*Frame2\" 0)(cx-gui-do cx-activate-tab-index \"Velocity Inlet*Frame2*Frame2\" 4)(cx-gui-do cx-activate-tab-index \"Velocity Inlet*Frame2*Frame2\" 0)(cx-gui-do cx-activate-tab-index \"Velocity Inlet*Frame2*Frame2\" 5)(cx-gui-do cx-activate-tab-index \"Velocity Inlet*Frame2*Frame2\" 0)(cx-gui-do cx-activate-tab-index \"Velocity Inlet*Frame2*Frame2\" 6)(cx-gui-do cx-activate-tab-index \"Velocity Inlet*Frame2*Frame2\" 0)(cx-gui-do cx-activate-tab-index \"Velocity Inlet*Frame2*Frame2\" 7)(cx-gui-do cx-activate-tab-index \"Velocity Inlet*Frame2*Frame2\" 0)(cx-gui-do cx-activate-tab-index \"Velocity Inlet*Frame2*Frame2\" 8)(cx-gui-do cx-activate-tab-index \"Velocity Inlet*Frame2*Frame2\" 0)(cx-gui-do cx-enable-apply-button \"Velocity Inlet\")(cx-gui-do cx-set-expression-entry \"Velocity Inlet*Frame2*Frame2*Frame1(Momentum)*Table1*Table8*ExpressionEntry1(Velocity Magnitude)\" '(\"1\" . 0))(cx-gui-do cx-activate-item \"Velocity Inlet*PanelButtons*PushButton1(OK)\")")
setup1.SendCommand(Command='(cx-gui-do cx-activate-item "Velocity Inlet*PanelButtons*PushButton2(Cancel)")')
setup1.SendCommand(Command='(cx-gui-do cx-set-list-tree-selections "NavigationPane*Frame2*Table1*List_Tree2" (list "Setup|Boundary Conditions"))')
setup1.SendCommand(Command='(cx-gui-do cx-set-list-tree-selections "NavigationPane*Frame2*Table1*List_Tree2" (list "Setup|Boundary Conditions"))(cx-gui-do cx-activate-item "NavigationPane*Frame2*Table1*List_Tree2")')
setup1.SendCommand(Command='(cx-gui-do cx-set-list-tree-selections "NavigationPane*Frame2*Table1*List_Tree2" (list "Setup|Boundary Conditions"))')
setup1.SendCommand(Command='(cx-gui-do cx-activate-item "Boundary Conditions*Table1*Table3*Table4*Table2*ButtonBox1*PushButton2(Profiles)")')
setup1.SendCommand(Command="(cx-gui-do cx-activate-item \"Profiles*Table7*Table1*PushButton1(Read)\")(cx-gui-do cx-set-file-dialog-entries \"Select File\" '( \"D:/Master/Thesis/AnsysFluentAutomationTest/InletProfile_InputData/inflow_profiles_Test10_New\") \"All Files (*)\")")
setup1.SendCommand(Command='(cx-gui-do cx-activate-item "Profiles*PanelButtons*PushButton1(OK)")')
setup1.SendCommand(Command="(cx-gui-do cx-set-list-selections \"Boundary Conditions*Table1*List2(Zone)\" '( 0))(cx-gui-do cx-activate-item \"Boundary Conditions*Table1*List2(Zone)\")")
setup1.SendCommand(Command='(cx-gui-do cx-activate-item "Boundary Conditions*Table1*Table3*Table4*ButtonBox1*PushButton1(Edit)")')
setup1.SendCommand(Command="(cx-gui-do cx-set-list-selections \"Velocity Inlet*Frame2*Frame2*Frame1(Momentum)*Table1*DropDownList6(Velocity Specification Method)\" '( 1))(cx-gui-do cx-enable-apply-button \"Velocity Inlet\")")
setup1.SendCommand(Command='(cx-gui-do cx-activate-item "Velocity Inlet*Frame2*Frame2*Frame1(Momentum)*Table1*DropDownList6(Velocity Specification Method)")')
setup1.SendCommand(Command="(cx-gui-do cx-set-expression-entry \"Velocity Inlet*Frame2*Frame2*Frame1(Momentum)*Table1*Table16*ExpressionEntry1(X-Velocity)\" '(\"velocity u\" . 3))(cx-gui-do cx-set-expression-entry \"Velocity Inlet*Frame2*Frame2*Frame1(Momentum)*Table1*Table17*ExpressionEntry1(Y-Velocity)\" '(\"velocity v\" . 3))(cx-gui-do cx-set-expression-entry \"Velocity Inlet*Frame2*Frame2*Frame1(Momentum)*Table1*Table18*ExpressionEntry1(Z-Velocity)\" '(\"velocity w\" . 3))(cx-gui-do cx-activate-item \"Velocity Inlet*PanelButtons*PushButton1(OK)\")")
setup1.SendCommand(Command='(cx-gui-do cx-activate-item "Velocity Inlet*PanelButtons*PushButton2(Cancel)")')
setup1.SendCommand(Command='(cx-gui-do cx-set-list-tree-selections "NavigationPane*Frame2*Table1*List_Tree2" (list ))(cx-gui-do cx-set-list-tree-selections "NavigationPane*Frame2*Table1*List_Tree2" (list "Setup|Materials|Fluid|air"))')
setup1.SendCommand(Command='(cx-gui-do cx-set-list-tree-selections "NavigationPane*Frame2*Table1*List_Tree2" (list "Setup|Materials|Fluid|air"))(cx-gui-do cx-activate-item "NavigationPane*Frame2*Table1*List_Tree2")')
setup1.SendCommand(Command="(cx-gui-do cx-set-list-tree-selections \"NavigationPane*Frame2*Table1*List_Tree2\" (list \"Setup|Materials|Fluid|air\"))(cx-gui-do cx-set-real-entry-list \"Create/Edit Materials*RealEntry10\" '( 1000))(cx-gui-do cx-set-real-entry-list \"Create/Edit Materials*RealEntry16\" '( 0.0035))(cx-gui-do cx-set-real-entry-list \"Create/Edit Materials*RealEntry16\" '( 0.00035))(cx-gui-do cx-set-text-entry \"Create/Edit Materials*Table1*Frame1*Table1*TextEntry1(Name)\" \"blood\")")
setup1.SendCommand(Command='(cx-gui-do cx-activate-item "Create/Edit Materials*PanelButtons*PushButton3(Change/Create)")(cx-gui-do cx-activate-item "Question*OK")')
setup1.SendCommand(Command='(cx-gui-do cx-activate-item "Create/Edit Materials*PanelButtons*PushButton1(Close)")')
setup1.SendCommand(Command="(cx-gui-do cx-activate-item \"MenuBar*ExportSubMenu*Case...\")(cx-
```

```
gui-do cx-set-file-dialog-entries \"Select File\" '( \"C:/Users/admin/Desktop/CFMeshTest10.cas.h5\") \"CFF Case Files (*.cas.h5 )\")")
setup1.SendCommand(Command='(cx-gui-do cx-activate-item "MenuBar*FileMenu*Close Fluent")')
system1 = GetSystem(Name="FLTG")
system1.Delete()


a=[11,12,13,14]
for x in a:
    ImportCommand = "(%py-exec \"workflow.TaskObject['Import Geometry'].Arguments.setState({r'FileFormat': r'Mesh',r'ImportCadPreferences': {r'CISeparation': r'region',},r'MeshFileName': r'E:/OpenFOAM/CFMesh_FluentSetupMeshGenerator/fluentInterface/CFMeshTest" + str(x) + ".msh',r'MeshUnit': r'mm',})\")"
    ExportCommand = "(cx-gui-do cx-activate-item \"MenuBar*ExportSubMenu*Case...\")(cx-gui-do cx-set-file-dialog-entries \"Select File\" '( \"C:/Users/admin/Desktop/CFMeshTest" + str(x) + ".cas.h5\") \"CFF Case Files (*.cas.h5 )\")"
    template1 = GetTemplate(TemplateName="FLTG")
    system1 = template1.CreateSystem()
    setup1 = system1.GetContainer(ComponentName="Setup")
    fluentLauncherSettings1 = setup1.GetFluentLauncherSettings()
    fluentLauncherSettings1.SetEntityProperties(Properties=Set(EnvPath={}, RunParallel=True, NumberOfProcessorsMeshing=4, NumberOfProcessors=4))
    tGridData1 = GetDataEntity("/Mesh/TGridData:TGridData")
    tGridData1.SetEntityProperties(Properties=Set(RunParallel=True, NumberOfProcs=4))
    mesh1 = system1.GetContainer(ComponentName="Mesh")
    Fluent.Edit(Container=mesh1)
    setup1.SendCommand(Command='(cx-gui-do cx-activate-tab-index "NavigationPane*Frame1(TreeTab)" 0)(cx-gui-do cx-activate-tab-index "NavigationPane*Frame1(TreeTab)" 1)')
    setup1.SendCommand(Command='/file/set-tui-version "22.2"(cx-gui-do cx-activate-tab-index "NavigationPane*Frame1(TreeTab)" 0)(cx-gui-do cx-activate-item "Key Behavioral Changes*PanelButtons*PushButton1(OK)")')
    setup1.SendCommand(Command='(%py-exec "preferences.General.KeyBehavioralChangesMessage.setState(True)")')
    setup1.SendCommand(Command="(%py-exec \"workflow.InitializeWorkflow(WorkflowType=r'Watertight Geometry')\")")
    setup1.SendCommand(Command="(%py-exec \"meshing.GlobalSettings.LengthUnit.setState(r'mm')\")")
    setup1.SendCommand(Command="(%py-exec \"meshing.GlobalSettings.AreaUnit.setState(r'mm^2')\")")
    setup1.SendCommand(Command="(%py-exec \"meshing.GlobalSettings.VolumeUnit.setState(r'mm^3')\")")
    setup1.SendCommand(Command=ImportCommand)
    setup1.SendCommand(Command="(%py-exec \"workflow.TaskObject['Import Geometry'].Execute()\")")
    setup1.SendCommand(Command="(%py-exec \"workflow.TaskObject['Add Local Sizing'].AddChildToTask()\")")
    setup1.SendCommand(Command="(%py-exec \"workflow.TaskObject['Add Local Sizing'].Execute()\")")
    setup1.SendCommand(Command="(%py-exec \"workflow.TaskObject['Generate the Surface Mesh'].Execute()\")")
    setup1.SendCommand(Command="(%py-exec \"workflow.TaskObject['Describe Geometry'].UpdateChildTasks(SetupTypeChanged=False)\")")
    setup1.SendCommand(Command="(%py-exec \"workflow.TaskObject['Describe Geometry'].Arguments.setState({r'SetupType': r'The geometry consists of only fluid regions with no voids',})\")")
    setup1.SendCommand(Command="(%py-exec \"workflow.TaskObject['Describe Geometry'].UpdateChildTasks(SetupTypeChanged=True)\")")
    setup1.SendCommand(Command="(%py-exec \"workflow.TaskObject['Describe Geometry'].Execute()\")")
    setup1.SendCommand(Command="(%py-exec \"workflow.TaskObject['Update Boundaries'].Execute()\")")
    setup1.SendCommand(Command="(%py-exec \"workflow.TaskObject['Update Regions'].Execute()\")")
    setup1.SendCommand(Command="(%py-exec \"workflow.TaskObject['Add Boundary Layers'].Arguments.setState({r'NumberOfLayers': 10,})\")")
    setup1.SendCommand(Command="(%py-exec \"workflow.TaskObject['Add Boundary Layers'].AddChildToTask()\")")
    setup1.SendCommand(Command="(%py-exec \"workflow.TaskObject['Add Boundary Layers'].InsertCompoundChildTask()\")")
    setup1.SendCommand(Command="(%py-exec \"workflow.TaskObject['smooth-transition_1'].Arguments.setState({r'BLControlName': r'smooth-transition_1',r'NumberOfLayers': 10,})\")")
    setup1.SendCommand(Command="(%py-exec \"workflow.TaskObject['Add Boundary Layers'].Arguments.setState({})\")")
    setup1.SendCommand(Command="(%py-exec \"workflow.TaskObject['smooth-transition_1'].Execute()\")")
    setup1.SendCommand(Command="(%py-exec \"workflow.TaskObject['Generate the Volume Mesh'].Arguments.setState({r'VolumeFillControls': {r'GrowthRate': 1.05,r'TetPolyMaxCellLength':
```

```
      0.00042,},})\")")
  setup1.SendCommand(Command="(%py-exec \"workflow.TaskObject['Generate the Volume Mesh'].
      Execute()\")")
  setup1.SendCommand(Command='(cx-gui-do cx-activate-item "Ribbon*Frame1*Frame2(Task Page)*
      Table1*Table3(Solution)*PushButton1(Switch to Solution)")(cx-gui-do cx-activate-item "
      Question*OK")(cx-gui-do cx-activate-tab-index "NavigationPane*Frame1(TreeTab)" 1)')
  setup1.SendCommand(Command="(newline)")
  setup1.SendCommand(Command='(cx-gui-do cx-set-list-tree-selections "NavigationPane*Frame2*
      Table1*List_Tree2" (list "Setup|Boundary Conditions|Inlet|inlet (velocity-inlet, id=10)"))
      ')
  setup1.SendCommand(Command='(cx-gui-do cx-set-list-tree-selections "NavigationPane*Frame2*
      Table1*List_Tree2" (list "Setup|Boundary Conditions|Inlet|inlet (velocity-inlet, id=10)"))
      (cx-gui-do cx-activate-item "NavigationPane*Frame2*Table1*List_Tree2")')
  setup1.SendCommand(Command="(cx-gui-do cx-set-list-tree-selections \"NavigationPane*Frame2*
      Table1*List_Tree2\" (list \"Setup|Boundary Conditions|Inlet|inlet (velocity-inlet, id=10)
      \"))(cx-gui-do cx-activate-tab-index \"Velocity Inlet*Frame2*Frame2\" 0)(cx-gui-do cx-
      activate-tab-index \"Velocity Inlet*Frame2*Frame2\" 1)(cx-gui-do cx-activate-tab-index \"
      Velocity Inlet*Frame2*Frame2\" 0)(cx-gui-do cx-activate-tab-index \"Velocity Inlet*Frame2*
      Frame2\" 2)(cx-gui-do cx-activate-tab-index \"Velocity Inlet*Frame2*Frame2\" 0)(cx-gui-do
      cx-activate-tab-index \"Velocity Inlet*Frame2*Frame2\" 3)(cx-gui-do cx-activate-tab-index
      \"Velocity Inlet*Frame2*Frame2\" 0)(cx-gui-do cx-activate-tab-index \"Velocity Inlet*
      Frame2*Frame2\" 4)(cx-gui-do cx-activate-tab-index \"Velocity Inlet*Frame2*Frame2\" 0)(cx-
      gui-do cx-activate-tab-index \"Velocity Inlet*Frame2*Frame2\" 5)(cx-gui-do cx-activate-tab
      -index \"Velocity Inlet*Frame2*Frame2\" 0)(cx-gui-do cx-activate-tab-index \"Velocity
      Inlet*Frame2*Frame2\" 6)(cx-gui-do cx-activate-tab-index \"Velocity Inlet*Frame2*Frame2\"
      0)(cx-gui-do cx-activate-tab-index \"Velocity Inlet*Frame2*Frame2\" 7)(cx-gui-do cx-
      activate-tab-index \"Velocity Inlet*Frame2*Frame2\" 0)(cx-gui-do cx-activate-tab-index \"
      Velocity Inlet*Frame2*Frame2\" 8)(cx-gui-do cx-activate-tab-index \"Velocity Inlet*Frame2*
      Frame2\" 0)(cx-gui-do cx-enable-apply-button \"Velocity Inlet\")(cx-gui-do cx-set-
      expression-entry \"Velocity Inlet*Frame2*Frame2*Frame1(Momentum)*Table1*Table8*
      ExpressionEntry1(Velocity Magnitude)\" '(\"1\" . 0))(cx-gui-do cx-activate-item \"Velocity
       Inlet*PanelButtons*PushButton1(OK)\")")
  setup1.SendCommand(Command='(cx-gui-do cx-activate-item "Velocity Inlet*PanelButtons*
      PushButton2(Cancel)")')
  setup1.SendCommand(Command='(cx-gui-do cx-set-list-tree-selections "NavigationPane*Frame2*
      Table1*List_Tree2" (list "Setup|Boundary Conditions"))')
  setup1.SendCommand(Command='(cx-gui-do cx-set-list-tree-selections "NavigationPane*Frame2*
      Table1*List_Tree2" (list "Setup|Boundary Conditions"))(cx-gui-do cx-activate-item "
      NavigationPane*Frame2*Table1*List_Tree2")')
  setup1.SendCommand(Command='(cx-gui-do cx-set-list-tree-selections "NavigationPane*Frame2*
      Table1*List_Tree2" (list "Setup|Boundary Conditions"))')
  setup1.SendCommand(Command='(cx-gui-do cx-activate-item "Boundary Conditions*Table1*Table3*
      Table4*Table2*ButtonBox1*PushButton2(Profiles)")')
  setup1.SendCommand(Command="(cx-gui-do cx-activate-item \"Profiles*Table7*Table1*PushButton1
      (Read)\")(cx-gui-do cx-set-file-dialog-entries \"Select File\" '( \"D:/Master/Thesis/
      AnsysFluentAutomationTest/InletProfile_InputData/inflow_profiles_Test10_New\") \"All Files
       (*)\")")
  setup1.SendCommand(Command='(cx-gui-do cx-activate-item "Profiles*PanelButtons*PushButton1(
      OK)")')
  setup1.SendCommand(Command="(cx-gui-do cx-set-list-selections \"Boundary Conditions*Table1*
      List2(Zone)\" '( 0))(cx-gui-do cx-activate-item \"Boundary Conditions*Table1*List2(Zone)
      \")")
  setup1.SendCommand(Command='(cx-gui-do cx-activate-item "Boundary Conditions*Table1*Table3*
      Table4*ButtonBox1*PushButton1(Edit)")')
  setup1.SendCommand(Command="(cx-gui-do cx-set-list-selections \"Velocity Inlet*Frame2*Frame2
      *Frame1(Momentum)*Table1*DropDownList6(Velocity Specification Method)\" '( 1))(cx-gui-do
      cx-enable-apply-button \"Velocity Inlet\")")
  setup1.SendCommand(Command='(cx-gui-do cx-activate-item "Velocity Inlet*Frame2*Frame2*Frame1
      (Momentum)*Table1*DropDownList6(Velocity Specification Method)")')
  setup1.SendCommand(Command="(cx-gui-do cx-set-expression-entry \"Velocity Inlet*Frame2*
      Frame2*Frame1(Momentum)*Table1*Table16*ExpressionEntry1(X-Velocity)\" '(\"velocity u\" .
      3))(cx-gui-do cx-set-expression-entry \"Velocity Inlet*Frame2*Frame2*Frame1(Momentum)*
      Table1*Table17*ExpressionEntry1(Y-Velocity)\" '(\"velocity v\" . 3))(cx-gui-do cx-set-
      expression-entry \"Velocity Inlet*Frame2*Frame2*Frame1(Momentum)*Table1*Table18*
      ExpressionEntry1(Z-Velocity)\" '(\"velocity w\" . 3))(cx-gui-do cx-activate-item \"
      Velocity Inlet*PanelButtons*PushButton1(OK)\")")
  setup1.SendCommand(Command='(cx-gui-do cx-activate-item "Velocity Inlet*PanelButtons*
      PushButton2(Cancel)")')
  setup1.SendCommand(Command='(cx-gui-do cx-set-list-tree-selections "NavigationPane*Frame2*
      Table1*List_Tree2" (list ))(cx-gui-do cx-set-list-tree-selections "NavigationPane*Frame2*
      Table1*List_Tree2" (list "Setup|Materials|Fluid|air"))')
  setup1.SendCommand(Command='(cx-gui-do cx-set-list-tree-selections "NavigationPane*Frame2*
      Table1*List_Tree2" (list "Setup|Materials|Fluid|air"))(cx-gui-do cx-activate-item "
      NavigationPane*Frame2*Table1*List_Tree2")')
  setup1.SendCommand(Command="(cx-gui-do cx-set-list-tree-selections \"NavigationPane*Frame2*
      Table1*List_Tree2\" (list \"Setup|Materials|Fluid|air\"))(cx-gui-do cx-set-real-entry-list
```

```
\"Create/Edit Materials*RealEntry10\" '( 1000))(cx-gui-do cx-set-real-entry-list \"Create
/Edit Materials*RealEntry16\" '( 0.0035))(cx-gui-do cx-set-real-entry-list \"Create/Edit
Materials*RealEntry16\" '( 0.00035))(cx-gui-do cx-set-text-entry \"Create/Edit Materials*
Table1*Frame1*Table1*TextEntry1(Name)\" \"blood\")")
setup1.SendCommand(Command='(cx-gui-do cx-activate-item "Create/Edit Materials*PanelButtons*
  PushButton3(Change/Create)")(cx-gui-do cx-activate-item "Question*OK")')
setup1.SendCommand(Command='(cx-gui-do cx-activate-item "Create/Edit Materials*PanelButtons*
  PushButton1(Close)")')
setup1.SendCommand(Command=ExportCommand)
setup1.SendCommand(Command='(cx-gui-do cx-activate-item "MenuBar*FileMenu*Close Fluent")')
system1 = GetSystem(Name="FLTG")
system1.Delete()
```

B.2 Fluent journal file for cluster

```
;Reading in the case file
file/read-case 20_Profile_436_FluentCase.cas.h5
;
;hybrid initialising the system
/solve/init/hyb-init
;
;Setting the transient time step size
/solve/set/time-step 0.001
;
;Setting the number of time-steps (first number) and the max
/solve/dual-time-iterate 5000 500
;
;Writing the final data file (overwriting if required)
;file/write-data fullcase.dat.gz
;
;Exit Fluent
/exit ok
```

C Inflow profile mapping related Python code

C.1 Code for mapping inflow profile to inputted shape [69]

```python
import sys
import os
import os.path as osp
import numpy as np
from glob import glob
import pyvista as pv

import utils as ut

counter = 1
hardDR=0.1
outputDir = r'OutPutMappingData' # path for saving resampled .vtp files
saveName = 'TestMap_00'   # filename of resamples .vtp files
source_profile_dir = r'data/mean_profile' # directory containing .vtp files associated to a 4D profile
target_profile_fn = r'InletSTL_TestData/inlet_00.vtp'  # can be a .stl, .vtk or .vtp file

List=['010','077','089','099','102','103','123','146','195','205','215','272','284','307','331','371','384','411','424','436']

for i in range(0,20,1):
#for i in range(10,16,1):

    # ------------------------------------------------------------------------------------------------------

    ## Options
    iCounter=i
    print('Starting with iteration',str(iCounter),'out of 19')
    counter=List[i]
    outputDir = r'OutPutMappingData' + str(counter) # path for saving resampled .vtp files
    saveName = 'FinalProfile' + str(counter)   # filename of resamples .vtp files
    source_profile_dir = r'data_Final/' + str(counter) # directory containing .vtp files associated to a 4D profile
    #target_profile_fn = r'InletSTL_TestData/inlet2.stl'
    target_profile_fn = r'InletSTL_TestData/inlet_0010.vtp'  # can be a .stl, .vtk or .vtp file
    flip_normals = False # usually set to True, but might have to change depending on target plane orientation
    #--------------------
    target_plane = pv.read(target_profile_fn)
    target_pts = target_plane.points
    index_min = min(range(len(target_pts[:,0])), key=target_pts[:,1].__getitem__)
    #---------------------
    leftmost_idx_on_target = index_min      # index of the leftmost point in the target plane w.r.t the subject
    intp_options = {
        'zero_boundary_dist': 0.5, # percentage of border with zero velocity (smooth damping at the border)
        'zero_backflow': True, # set all backflow components to zero
        'kernel': 'linear', # RBF interpolation kernel (linear is recommended)
        'smoothing': 0.5, # interpolation smoothing, range recommended [0, 2]
        'degree': 0,
        'hard_noslip': True} # degree of polynomial added to the RBF interpolation matrix


    # ------------------------------------------------------------------------------------------------------

    ## Read data
    source_profiles = [pv.read(i) for i in sorted(glob(osp.join(source_profile_dir, '*.vtp')))]
    target_plane = pv.read(target_profile_fn)

    num_frames = len(source_profiles)
    source_pts = [source_profiles[k].points for k in range(num_frames)]
    source_coms = [source_pts[k].mean(0) for k in range(num_frames)]
    target_pts = target_plane.points
    target_com = target_pts.mean(0)
    target_normal = target_plane.compute_normals()['Normals'].mean(0)
    normals = [source_profiles[k].compute_normals()['Normals'].mean(0) for k in range(
```

```
    num_frames)]
    if flip_normals: normals = [normals[k] * -1 for k in range(num_frames)]


    #
    ---------------------------------------------------------------------------------------------------
    ## Align source to target

    # center at origin for simplicity
    target_pts -= target_com
    source_pts = [source_pts[k] - source_coms[k] for k in range(num_frames)]

    # normalize w.r.t. max coordinate norm
    targetmax = np.max(np.sqrt(np.sum(target_pts ** 2, axis=1)))
    pts = [source_pts[k] * targetmax for k in range(num_frames)]

    # rotate to align normals
    Rots = [ut.rotation_matrix_from_vectors(normals[k], target_normal) for k in range(
    num_frames)]
    pts = [Rots[k].dot(pts[k].T).T for k in range(num_frames)]
    vel = [Rots[k].dot(source_profiles[k]['Velocity'].T).T for k in range(num_frames)]

    # second rotation to ensure consistent in-plane alignment
    lm_ids = [np.argmax(source_pts[k][:, 0]) for k in range(num_frames)]
    Rots_final = [ut.rotation_matrix_from_vectors(pts[k][lm_ids[k], :], target_pts[
    leftmost_idx_on_target, :]) for k in range(num_frames)]
    pts = [Rots_final[k].dot(pts[k].T).T for k in range(num_frames)]
    vel = [Rots_final[k].dot(vel[k].T).T for k in range(num_frames)]


    # create new polydatas
    aligned_planes = [source_profiles[k].copy() for k in range(num_frames)]
    for k in range(num_frames):
        aligned_planes[k].points = pts[k]
        aligned_planes[k]['Velocity'] = vel[k]

    # spatial interpolation
    interp_planes = ut.interpolate_profiles(aligned_planes, target_pts, intp_options,
    target_com, hardDR)

    # recenter
    for k in range(num_frames):
        interp_planes[k].points += target_com


    #
    ---------------------------------------------------------------------------------------------------
    ## Save profiles to .vtp
    os.makedirs(outputDir, exist_ok=True)
    for k in range(num_frames):
        interp_planes[k].save(osp.join(outputDir, saveName + '_{:02d}.vtp'.format(k)))
```

C.2 Code for writing velocity profiles for Fluent

```python
import sys
import os
import os.path as osp
import numpy as np
import pyvista as pv
from glob import glob
from tqdm import tqdm
from scipy.interpolate import interp1d
import shutil

outputDir = r'SolverWriteOutput'

List=['010','077','089','099','102','103','123','146','195','205','215','272','284','307','331','371','384','411','424','436']

for i in range(0,20,1):

    # ----------------------------------------------------------------------------------------------------
    ## Options
    iCounter=i
    print('Starting with iteration',str(iCounter),'out of 19')
    counter=List[i]
    profilesDir = r'OutPutMappingData' + str(counter)
    saveName = 'FinalFluentProfile_' + str(counter)
    #cfd_delta_t = 0.001  # simulation time steps
    cfd_delta_t = 1  # simulation time steps
    cardiac_cycle_period = 1.0
    time_interpolation = 'linear' # can be linear, nearest, quadratic, ..., cubic
    solver = 'fluent' # can be star, ...!TODO add CFX, OpenFoam and SimVascular


    # ----------------------------------------------------------------------------------------------------
    ## Prepare variables
    interp_planes = [pv.read(fn) for fn in sorted(glob(osp.join(profilesDir, '*.vtp')))]
    num_frames = len(interp_planes)

    os.makedirs(outputDir, exist_ok=True)

    tcfd = np.arange(0, cardiac_cycle_period, cfd_delta_t)
    t4df = np.linspace(0, cardiac_cycle_period, num_frames)
    pos = interp_planes[0].points
    npts = pos.shape[0]
    vel4df = np.array([interp_planes[k]['Velocity'] for k in range(len(interp_planes))])
    #velcfd = interp1d(t4df, vel4df, axis=0, kind=time_interpolation)(tcfd)


    # ----------------------------------------------------------------------------------------------------
    ## Write files for solver

# =============================================================================
#     if solver == 'star':
#         # write .csv for star-ccm+
#         with open(osp.join(profilesDir, saveName + '.csv'), 'w') as fn:
#             riga = 'X,Y,Z'
#             for j in range(len(tcfd)):
#                 riga += ',u(m/s)[t={}s],v(m/s)[t={}s],w(m/s)[t={}s]'.format(tcfd[j], tcfd[j], tcfd[j])
#             riga += '\n'
#             fn.write(riga)
#             for i in tqdm(range(len(pos))):
#                 riga = '{},{},{}'.format(pos[i, 0], pos[i, 1], pos[i, 2])
#                 for j in range(len(tcfd)):
#                     riga += ',{},{},{}'.format(velcfd[j, i, 0], velcfd[j, i, 1], velcfd[j, i, 2])
#                 riga += '\n'
#                 fn.write(riga)
# =============================================================================

```

```
    if solver == 'fluent':
        # write .prof for ansys fluent
        xx, yy, zz = pos[:, 0].tolist(), pos[:, 1].tolist(), pos[:, 2].tolist()
        fu = np.swapaxes(vel4df[:, :, 0], 0, 1)
        fv = np.swapaxes(vel4df[:, :, 1], 0, 1)
        fw = np.swapaxes(vel4df[:, :, 2], 0, 1)
        for i in tqdm(range(len(tcfd))):
            with open(osp.join(profilesDir, saveName), 'w') as fn:
                fn.write('((velocity point {})\n'.format(npts))
                fn.write('(x\n')
                for xi in xx:
                    fn.write(str(xi) + '\n')
                fn.write(')\n')
                fn.write('(y\n')
                for yi in yy:
                    fn.write(str(yi) + '\n')
                fn.write(')\n')
                fn.write('(z\n')
                for zi in zz:
                    fn.write(str(zi) + '\n')
                fn.write(')\n')
                fn.write('(u\n')
                for ui in fu[:, i]:
                    fn.write(str(ui) + '\n')
                fn.write(')\n')
                fn.write('(v\n')
                for vi in fv[:, i]:
                    fn.write(str(vi) + '\n')
                fn.write(')\n')
                fn.write('(w\n')
                for wi in fw[:, i]:
                    fn.write(str(wi) + '\n')
                fn.write(')\n')
                fn.write(')')


#Extra lines for transfering output profiles into a single folder (The SolverWriteOutput folder)
    profilesDirLoopTransfer = r'OutPutMappingData' + str(counter) + '/FinalFluentProfile_' + str(counter)
    profilesDirLoopTransferOutput = r'SolverWriteOutput/FinalFluentProfile_' + str(counter)
    shutil.move(profilesDirLoopTransfer, profilesDirLoopTransferOutput)
```

D All WSS data and inflow variable data in a nice table

Profile number from dataset	10	77	89	99	102	103	123	146	195	205
FJA (degrees)	30.67	42.52	15.63	44.72	30.66	27.91	40.34	23.79	47.59	39.16
CJ-FJA (degrees)	14.45	10.87	12.44	7.97	10.37	15.34	15.73	18.31	20.93	25.88
Secondary angle (degrees)	0.00	1.18	13.09	-3.84	58.17	27.30	7.68	24.79	24.25	29.83
Flow rate (L/s)	0.155	0.132	0.201	0.132	0.188	0.188	0.144	0.207	0.161	0.181
Eccentric distance (mm)	0.96	1.47	0.80	1.82	1.26	1.12	2.07	1.16	1.21	1.80
WSS 80^{th} percentile (Pa)	5.34	5.27	7.79	5.59	10.19	7.45	6.55	8.72	8.33	8.25
81^{st}	5.55	5.54	8.09	5.84	10.51	7.78	6.73	8.95	8.50	8.43
82^{nd}	5.78	5.80	8.41	6.11	10.84	8.12	6.96	9.21	8.68	8.63
83^{rd}	6.04	6.09	8.73	6.41	11.16	8.46	7.21	9.48	8.87	8.84
84^{th}	6.30	6.43	9.08	6.77	11.49	8.84	7.47	9.77	9.05	9.03
85^{th}	6.54	6.79	9.37	7.16	11.83	9.18	7.74	10.09	9.27	9.23
86^{th}	6.82	7.19	9.71	7.61	12.20	9.51	8.03	10.42	9.49	9.46
87^{th}	7.19	7.62	10.05	8.05	12.59	9.84	8.37	10.80	9.73	9.68
88^{th}	7.65	8.11	10.41	8.50	13.01	10.20	8.74	11.21	9.99	9.94
89^{th}	8.12	8.63	10.80	9.03	13.51	10.57	9.14	11.68	10.26	10.23
90^{th}	8.66	9.20	11.18	9.55	14.03	10.95	9.53	12.18	10.57	10.56
91^{st}	9.23	9.90	11.62	10.05	14.59	11.35	9.93	12.68	10.88	10.88
92^{nd}	9.80	10.64	12.08	10.65	15.29	11.76	10.37	13.24	11.21	11.23
93^{rd}	10.40	11.62	12.58	11.39	16.05	12.21	10.84	13.77	11.57	11.64
94^{th}	11.09	12.71	13.18	12.23	16.98	12.68	11.32	14.31	11.96	12.07
95^{th}	11.68	13.90	13.86	13.34	18.05	13.21	11.88	14.82	12.44	12.52
96^{th}	12.35	15.17	14.62	14.55	19.11	13.88	12.49	15.39	12.98	12.98
97^{th}	13.13	16.52	15.47	15.84	20.38	14.77	13.31	15.97	13.74	13.49
98^{th}	13.99	17.86	16.50	17.22	21.91	16.13	14.37	16.61	14.90	14.17
99^{th}	15.11	19.78	18.03	19.17	24.15	17.72	15.71	17.67	16.46	15.14
Peak WSS (Pa)	18.90	26.71	22.42	25.41	31.67	22.20	19.96	20.94	26.34	20.58

Table 11: Table showing profile numbers from the dataset of Saitta et al. [69], inflow variable data and ascending aortic WSS results represented as percentile data of the first 10 profiles

Profile number from dataset	215	272	284	307	331	371	384	411	424	436
FJA (degrees)	19.32	27.09	31.12	31.31	27.12	19.04	22.51	37.22	30.07	32.53
CJ-FJA (degrees)	11.96	19.46	20.75	26.45	20.93	17.70	21.01	16.31	20.48	11.22
Secondary angle (degrees)	24.41	-14.42	28.49	46.75	33.96	34.55	20.15	-6.71	2.87	75.82
Flow rate (L/s)	0.209	0.227	0.181	0.174	0.209	0.242	0.234	0.181	0.189	0.157
Eccentric distance (mm)	0.88	1.89	0.56	0.66	1.03	0.81	1.01	2.31	1.65	0.68
WSS 80^{th} percentile (Pa)	7.39	10.04	7.82	8.46	9.33	8.26	8.89	8.44	8.48	7.76
81^{st}	7.72	10.30	8.01	8.72	9.63	8.50	9.05	8.76	8.68	8.04
82^{nd}	8.05	10.58	8.22	8.98	9.94	8.76	9.24	9.09	8.89	8.30
83^{rd}	8.38	10.90	8.44	9.23	10.25	9.05	9.43	9.39	9.12	8.60
84^{th}	8.72	11.25	8.68	9.51	10.54	9.35	9.62	9.77	9.40	8.91
85^{th}	9.08	11.61	8.91	9.76	10.85	9.67	9.80	10.16	9.70	9.18
86^{th}	9.47	11.99	9.14	10.02	11.15	10.01	9.99	10.53	10.06	9.49
87^{th}	9.89	12.37	9.37	10.29	11.44	10.37	10.17	10.91	10.42	9.80
88^{th}	10.37	12.75	9.63	10.57	11.74	10.74	10.36	11.27	10.78	10.13
89^{th}	10.93	13.19	9.87	10.86	12.02	11.12	10.55	11.70	11.16	10.49
90^{th}	11.49	13.67	10.12	11.17	12.35	11.52	10.74	12.14	11.55	10.87
91^{st}	12.04	14.23	10.38	11.49	12.67	11.90	10.95	12.64	11.97	11.33
92^{nd}	12.63	14.91	10.64	11.79	13.02	12.26	11.16	13.21	12.44	11.82
93^{rd}	13.16	15.82	10.92	12.13	13.38	12.65	11.38	13.79	13.00	12.39
94^{th}	13.69	16.80	11.20	12.50	13.80	13.07	11.63	14.52	13.62	13.14
95^{th}	14.32	17.70	11.53	12.89	14.22	13.52	11.91	15.24	14.31	14.09
96^{th}	15.05	18.76	11.90	13.34	14.72	14.06	12.22	15.95	15.06	15.15
97^{th}	16.29	20.03	12.31	13.94	15.25	14.82	12.62	16.76	15.97	16.46
98^{th}	18.08	21.47	12.87	14.63	16.00	15.86	13.13	17.72	17.09	18.08
99^{th}	20.71	23.35	13.60	15.66	17.19	17.54	13.94	19.03	18.73	20.22
Peak WSS (Pa)	26.46	31.80	16.67	19.36	22.77	26.70	17.27	23.91	26.27	25.18

Table 12: Table showing data of the last 10 profiles

E Linear regression results for insignificant variables

Secondary angle and WSS Linear Regression	Significance level (p)	Linear regression slope coefficient	Standard error	R^2
80^{th} percentile WSS	0.15	0.020	0.014	0.11
82^{nd}	0.14	0.021	0.014	0.12
84^{th}	0.15	0.021	0.014	0.11
86^{th}	0.20	0.019	0.014	0.091
88^{th}	0.25	0.016	0.014	0.072
89^{th}	0.29	0.015	0.014	0.061
90^{th}	0.35	0.014	0.014	0.050
92^{nd}	0.52	0.0097	0.015	0.023
94^{th}	0.85	0.0033	0.017	0.0022
96^{th}	0.98	-0.00054	0.020	4.0E-05
98^{th}	0.98	-0.00062	0.025	3.3E-05
99^{th}	0.96	0.0016	0.030	0.00017

Table 13: Linear regression results for the secondary angle with various percentiles of WSS in the ascending aorta

Eccentricity and WSS Linear Regression	Significance level (p)	Linear regression slope coefficient	Standard error	R^2
80^{th} percentile WSS	0.86	-114	636	0.0018
82^{nd}	0.85	-125	644	0.0021
84^{th}	0.88	-103	647	0.0014
86^{th}	0.99	-8.32	649	9.1E-06
88^{th}	0.91	71.7	636.	0.00070
89^{th}	0.84	131	633	0.0024
90^{th}	0.77	190	633	0.0050
92^{nd}	0.57	381	657	0.018
94^{th}	0.32	748	730	0.055
96^{th}	0.21	1110	856	0.085
98^{th}	0.23	1340	1070	0.080
99^{th}	0.28	1410	1260	0.065

Table 14: Linear regression results for the eccentricity with various percentiles of WSS in the ascending aorta